Journal of Advanced Ceramics
2024, **13**(12): 1891–1918
https://doi.org/10.26599/JAC.2024.9220986
Review

Fluoride transparent ceramics for solid-state lasers: A review

Xiang Li[1,2], Chen Hu[1,3], Qiang Liu[2], Dariusz Hreniak[4], Jiang Li[1,3,✉]

[1] *Transparent Ceramics Research Center, Shanghai Institute of Ceramics, Chinese Academy of Sciences, Shanghai 201899, China*
[2] *School of Material Science and Engineering, Jiangsu University, Zhenjiang 212013, China*
[3] *Center of Materials Science and Optoelectronics Engineering, University of Chinese Academy of Sciences, Beijing 100049, China*
[4] *Institute of Low Temperature and Structure Research, Polish Academy of Sciences, Wroclaw 50-422, Poland*

Received: August 22, 2024; Revised: October 5, 2024; Accepted: October 13, 2024

© The Author(s) 2024. This is an open access article under the terms of the Creative Commons Attribution 4.0 International License (CC BY 4.0, http://creativecommons.org/licenses/by/4.0/).

Abstract: Fluoride laser ceramics, which are employed as amplification media in solid-state lasers, have attracted considerable attention because of their excellent optical properties combined with other material parameters important for these applications, making them highly versatile materials. In this review, the fabrication and properties of fluoride laser ceramics, including CaF_2, SrF_2, and BaF_2 ceramics, are comprehensively investigated. As the state-of-art analysis shows, while some ceramic materials of this type have shown promising properties suitable for practical applications, most still require further research in the field of basic research. Specifically, this article reviews the state of research, identifies issues and prevailing challenges, and outlines development trends for fluoride ceramics for solid-state laser applications. The information gathered here is an important compendium of knowledge both for researchers seeking to work in this field of science and as a source of the latest information for experienced professionals who are already continuing preimplementation work in this area.

Keywords: fluoride laser ceramics; solid lasers; optical quality; laser performance; transparent ceramics (TCs)

1 Introduction

Solid-state lasers have found widespread applications in metal processing, medical treatment, environmental monitoring systems, and various other fields, becoming almost a symbol of the scientific advances of our current technological civilization [1–5]. The key to achieving population inversion and optical amplification and consequently achieving efficient laser action is the amplification medium used [6]. In the past, owing to their native optical transparency, only single crystals and glasses with appropriate physical properties served as the primary media for laser amplification [7–9]. However, recent advancements in ceramic fabrication technologies have led to the emergence of transparent ceramics (TCs) with high optical quality, providing an attractive alternative to solid-state laser gain media [10–13]. Moreover, TCs offer numerous advantages over single crystals, including shorter production times and greater ease in achieving composite structures and complex shapes [14–16]. Additionally, TCs exhibit significantly better thermal performance than glasses do [17–19]. In addition to the appropriate specific physical properties, which primarily include low phonon energy, low melting points, negative thermo-optical coefficients, and low refractive indices, it is necessary to dope with appropriate dopants to obtain the final required spectroscopic characteristics of the host materials. Moreover, fluoride ceramics with fluorite structures offer the possibility of easy doping with luminescent ions in a wide range of concentrations, including rare earth ions (RE^{3+}), such as Yb^{3+}, Nd^{3+}, or Er^{3+}, which are important for solid-state laser materials [20–23]. Importantly, owing to the widely recognized facts above and the efforts put in by research groups worldwide, in recent years, innovations in manufacturing methods and the availability of increasingly advanced equipment have contributed to the exponential development of technologies for obtaining fluoride transparent ceramics with increasingly better performance. Summarizing the above facts, it can be said with certainty that fluoride transparent ceramics currently occupy a key position in the research and development of laser ceramics, as evidenced in this article, and at the same time, numerous reports in recent years confirm that expectations for these materials continue to exceed achievements, and the work on their further optimization still does not lose its pace.

✉ Corresponding author.
E-mail: lijiang@mail.sic.ac.cn

1.1 Solid laser gain medium materials

Currently, lasers are broadly categorized into five types: solid-state lasers, gas lasers, liquid (dye) lasers, semiconductor lasers, and free electron lasers [24]. Owing to their early development and notable advantages, including compactness, portability, accessibility to high-energy laser outputs, and cost-effectiveness, solid-state lasers are extensively employed in large-scale laser systems such as Shenguang III, the National Ignition Facility (NIF), and military weaponry [25,26]. The architecture of solid-state lasers typically comprises three components: a resonant cavity, a solid-state laser gain medium, and a pump source (Fig. 1). Among these, the laser gain medium plays a central role in achieving population inversion and optical amplification [27].

The main solid-state laser gain media commonly used today include single crystals, glasses, and ceramics with varying chemical compositions. In the six decades of robust advancements in solid-state lasers, laser single crystals and laser glasses have emerged as

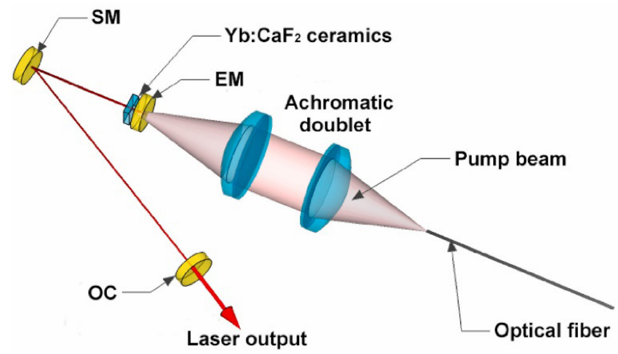

Fig. 1 Schematic diagram of Yb:CaF_2 laser. Reproduced with permission from Ref. [11], © Elsevier B.V. 2023.

pivotal gain media that have been extensively researched and utilized. Among laser single crystals, oxide crystals such as Nd:YAG [1,28], Yb:YAG [29,30], and Nd:YVO_4 [31,32] and fluoride crystals such as Nd:YLF [33,34], Yb:CaF_2 [35–37], Nd:CaF_2 [38,39], and Yb:SrF_2 [40–42] find application across various solid-state lasers spanning different power levels. Laser glasses, including phosphate glass [43–45], germanate glass [46–48], and tellurite glass [49–51] doped with diverse rare earth ions, have also garnered attention. In particular, Nd^{3+}-doped phosphate glass (Nd:glass) is popular in ultrastrong and ultrashort laser systems because of its sizable stimulated emission cross-section and low nonlinear refractive index [3,7,52–55].

While the preparation and utilization of the former two are well-established and widespread, they suffer from several challenging limitations, hindering their further advancement and application. For example, single-crystal fabrication entails lengthy cycles and high costs, with challenges in achieving high-concentration uniform doping of rare earth ions [56]. Glasses exhibit poor mechanical and thermal properties, impacting the laser's operational lifespan. Conversely, laser ceramics offer notable benefits such as superior thermal and mechanical characteristics, shorter fabrication cycles, and ease of shaping into complex forms and larger sizes [57–60], garnering significant attention from researchers.

1.2 Performance requirements for solid-state laser gain medium

The performance of solid-state laser gain media, pivotal components of solid-state lasers, significantly influences laser performance and quality. Consisting primarily of matrix materials and activated ions, these media rely on matrix materials meeting specific criteria to enable the generation of high-energy efficient lasers [61]. High-performance laser gain media necessitate specific characteristics in both activating ions and matrix materials:

(1) Optical quality

To minimize optical loss, laser materials must exhibit high optical quality and be devoid of internal pores or equivalent optical scattering centers [17,62].

(2) Mechanical properties

Laser materials should possess favorable mechanical properties to facilitate the fabrication of laser gain media of various shapes and sizes, accommodating diverse practical application environments [63]. Common configurations include thin sheets, zig-zag plates, rods, and planar waveguides [64].

(3) Thermal performance

Optimal thermal performance is crucial, as laser materials inevitably generate waste heat through nonradiative transitions during operation. Solid-state optical materials must exhibit excellent thermal conductivity to mitigate the thermal lensing effects induced by internal temperature gradients during high-power operation. Inadequate thermal conductivity and thermal shock resistance can exacerbate material susceptibility to damage, compromising the laser output quality [65].

(4) Activating ion selection

The selection of activating ions necessitates meticulous screening on the basis of the desired laser wavelength for the intended application. Additionally, achieving uniform doping throughout the matrix materials is essential for optimal performance [66].

Compared with glass, laser ceramics possess physical and chemical properties similar to those of single crystals, boasting superior mechanical and notably enhanced thermal properties. Additionally, they offer advantages such as lower production costs and facile preparation of large-sized and intricate samples. Consequently, they constitute an indispensable component of gain media in the design of new solid-state lasers. The ongoing refinement in preparation techniques for ceramic powders characterized by high purity and favorable sintering activity, coupled with the rapid evolution of sintering methodologies such as hot pressing (HP) sintering and hot isostatic pressing (HIP) sintering, has propelled the production of high-optical-quality laser TCs [67].

1.3 Development of laser ceramics and fluoride laser ceramics

In 1964, Hatch *et al.* [68] from Kodak achieved a milestone by successfully producing Dy:CaF_2 TCs through vacuum HP sintering technology, marking the initial laser output possible from ceramic lasers. However, owing to the low optical quality of ceramics, laser operation requires liquid helium temperatures to achieve output, resulting in a considerable performance gap compared with that of single crystals, leading to limited attention at that time.

In 1995, Ikesue and his team [10] accomplished a significant feat by fabricating high-optical-quality 1.1 at% Nd:YAG TCs utilizing high-purity Al_2O_3, Y_2O_3, and Nd_2O_3 powders through solid-state reaction sintering technology. They achieved continuous laser output at 1064 nm for the first time, with the lasing threshold and slope efficiency reaching 309 mW and 28%, respectively. Their laser performance rivaled that of Nd:YAG single crystals prepared via the pulling method, highlighting the vast potential of laser TCs as laser gain media. Building on this success, Ikesue *et al.* [69–72] delved deeper into the impact of the pore volume and scattering centers on the laser performance of Nd:YAG ceramics and compared the optical quality and laser performance across different Nd^{3+} concentrations [73]. These research outcomes significantly piqued researchers' interest in laser TCs. In 1999, Konoshima Chemical Company in Japan [74–76] utilized nanofabrication technology alongside vacuum sintering processes to fabricate high-quality Nd:YAG TCs, which boasted optical properties nearly indistinguishable from those of single crystals. Lu *et al.* [77] from the University of Electro-Communications in Japan spearheaded the development of a series of robust ceramic solid-state lasers using Nd:YAG ceramics sourced from Konoshima Chemical. These lasers achieve a remarkable slope efficiency of up to 55.5%, with output power scaling from an initial 31 W to kilowatts. By 2002, the laser output had surged to 1.46 kW [78–80]. Beyond Japan, USA intensified its exploration of ceramic solid-state lasers. In 2006, Lawrence Livermore National Laboratory (LLNL) achieved a continuous laser output of 67 kW, leveraging large-scale Nd:YAG transparent ceramics “flat noodles” (10 cm × 10 cm × 2 cm) provided by Konoshima Chemical Co. [81]. In 2009, Textron Defense Inc. [82] reached a milestone with the Nd:YAG ceramic laser, achieving a remarkable 100 kW laser output. Concurrently, Northrop Grumman [83] in USA achieved over 100 kW of laser output with a Yb:YAG ceramic laser in the same year.

In addition to garnet materials, sesquioxide materials (Y_2O_3, Lu_2O_3, and Sc_2O_3) play pivotal roles as constituents of laser transparent ceramic matrices [84–86]. Compared with YAG materials, sesquioxides boast superior thermal conductivity and offer distinct advantages in high-power solid-state lasers. Furthermore, sesquioxide ceramics entail lower preparation complexities than single crystals do [87]. The unique properties of rare earth ion-doped sesquioxide laser TCs have garnered significant interest among researchers worldwide. Beginning in 2001, Lu *et al.* [88] achieved notable success in this field by attaining a laser output with a slope efficiency of 32% in Nd:Y_2O_3 TCs via nanotechnology combined with vacuum sintering technology. Following this breakthrough, in 2002, Lu *et al.* [89] successfully prepared Yb:Y_2O_3 TCs, achieving continuous laser output at 1077 nm. This paved the way for the development of various high-quality sesquioxide-based laser TCs, such as Nd:Lu_2O_3, Yb:Lu_2O_3, and Yb:Sc_2O_3, which demonstrated continuous laser output in subsequent studies [4,90–95]. Notably, in 2021, the University of Stuttgart in Germany achieved a significant milestone by achieving continuous laser output with an optical-to-optical conversion efficiency of 60.3% and a power of 1190 W through Yb:Lu_2O_3 ceramic thin plate lasers [96]. Moreover, sesquioxide-based laser ceramics exhibit superior performance in ultrashort pulse lasers. For example, in 2009, the University of Electro-Communications achieved pulsed laser outputs of 68 and 53 fs using Yb:Y_2O_3 and Yb:Sc_2O_3 ceramic lasers, respectively [97,98]. Similarly, in 2017, Paradis *et al.* [99] in Switzerland accomplished a 35 fs ultrashort pulse laser output using Yb:Lu_2O_3 ceramic lasers in Kerr-lens mode locking.

Table 1 presents the physicochemical properties of common matrix materials that can be used as gain media for solid-state lasers [100–102]. Compared with common oxide transparent ceramics, fluoride transparent ceramics have significant application prospects in the field of solid-state lasers because of their excellent physicochemical properties. First, compared with oxide matrix materials, fluoride has a lower melting point, resulting in lower preparation costs and difficulties. Second, the low density of fluoride is beneficial for reducing the quality of solid-state lasers and achieving a lightweight design for laser devices. In addition, fluoride materials have a wide transmission band from deep ultraviolet to mid-infrared (MIR), which can be used as gain medium matrix materials for lasers of different wavelengths. At the same time, the phonon energy of fluoride materials is relatively low, which can effectively reduce the nonradiative transition probability of RE^{3+}, improve quantum efficiency, and, to some extent, reduce the generation of waste heat, thereby reducing the thermal load during laser operation. Finally, their unique negative thermal optical coefficient can effectively reduce the thermal lens effect during laser operation [103].

Fluoride ceramics, which serve as laser substrate materials, boast advantages such as low phonon energy, wide transmission bands, excellent mechanical and thermal properties, and low nonlinear refractive indices. Consequently, they have emerged as highly promising laser gain media, particularly in high-peak-power laser systems [15–18]. Notably, the inspiration and guidance provided by oxide transparent ceramics for the development of fluoride ceramics should not be ignored. By leveraging insights and techniques, such as fabrication techniques, additives and doping, microstructural control, and composite development from the development of oxide transparent ceramics, researchers have significantly enhanced the performance and applicability of fluoride ceramics.

In recent years, interest in rare earth ion-doped fluoride laser TCs has increased. The unique characteristics of fluoride ceramics, including their phonon energy, refractive index, and nonlinear refractive index, make them highly suitable as laser matrix materials. Fluoride-based laser ceramics also offer thermal conductivity comparable to that of fluoride laser crystals and possess advantages in fracture toughness and thermal shock resistance [104]. Simultaneously, they facilitate high-concentration uniform doping and the fabrication of large-sized and intricately shaped samples, rendering them highly promising as laser gain media. Fluoride-based laser ceramics currently under widespread study primarily include calcium fluoride and strontium fluoride [11]. In 2008, Basiev *et al.* [101] of the Russian Academy of Sciences synthesized CaF_2–SrF_2–YbF_3 TCs via the hot forging single-crystal method. These ceramics exhibited microhardness akin to that of CaF_2 single crystals prepared through the crucible descent technique, with a fracture toughness that was 1.75 times than that of single crystals. Additionally, the ceramic laser slope efficiency reached 45%, closely resembling that of Yb:CaF_2 single crystals at the time and 2.7 times that of Yb:SrF_2 single crystals (Fig. 2) [105]. Moreover, Basiev *et al.* [101] demonstrated that Nd:SrF_2 ceramics produced via the hot forging single-crystal method presented optical quality and laser performance on par with Nd:SrF_2 single crystals. In 2011, Pr:SrF_2 TCs were successfully fabricated by Basiev *et al.* [106] via the hot forming method, achieving a laser output of 639 nm in performance testing. Furthermore, in 2017, Jiang *et al.* [107] employed an optimized

Table 1 Properties of host materials for gain media in solid-state lasers at room temperature

Host material	CaF_2	SrF_2	YAG	Lu_2O_3
Lattice	Cubic	Cubic	Cubic	Cubic
Melting point (°C)	1380	1428	1940	2490
Density (g/cm^3)	3.18	4.24	4.55	9.42
Thermal expansion coefficient (10^{-6} K^{-1})	18.9	18.6	6.1	8.6
Thermal capacity, c_p (J/(g·K))	0.88	0.91	0.63	0.24
Thermal conductivity, κ (W/(m·K))	9.71	8.7	10.7	12.5
Transparency range (μm)	0.13–11	0.13–11.5	0.23–6.4	0.23–8
Refractive index	1.424 (1064)	1.432 (1060)	1.815 (1064)	1.911 (1000)
Phonon energy (cm^{-1})	328	280	850	612
Thermal–optic coefficient, dn/dT (10^{-6} K^{-1})	−12.7	−20	7.8–8.4	7.1

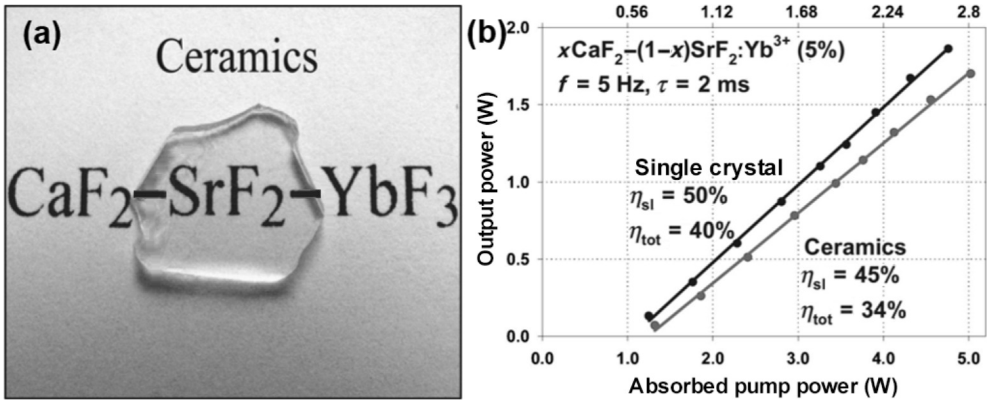

Fig. 2 (a) Photograph of CaF_2–SrF_2–YbF_3 laser ceramics. (b) Input–output characteristics of CaF_2–SrF_2–YbF_3 single crystal and ceramics under LD pumping measured under similar conditions. Reproduced with permission from Ref. [105], © Optical Society of America 2008.

hot forging single-crystal method to prepare Nd,Y:CaF_2 TCs with enhanced mechanical properties such as microhardness and fracture toughness, consequently achieving successful laser output. These findings underscore the promising potential of fluoride-based laser ceramics. However, the hot forging single-crystal method, which uses single crystals as starting materials, entails relatively high preparation costs for ceramics. To address this issue, Aubry *et al.* [108] from France employed the coprecipitation method in 2009 to synthesize 10 at% Yb:CaF_2 powders, followed by vacuum presintering and HIP posttreatment for the production of Yb:CaF_2 TCs. Despite these efforts, laser output was not achieved. In 2011, Mortier *et al.* [109] optimized Aubry's sintering technique, enhancing the optical quality of Yb:CaF_2 ceramics and successfully achieving laser oscillation. In 2017, the University of Electro-Communications of Japan collaborated with Nikon Co. to fabricate high-quality Yb,La:CaF_2 TCs through air presintering combined with HIP posttreatment [67]. These ceramics exhibited average grain sizes ranging from 3 to 4 μm, with extremely thin grain boundaries and minimal pore presence. In subsequent laser performance evaluations, these ceramics demonstrated a remarkable slope efficiency of 69.5% and a peak power output of 4.36 W, currently representing the best continuous laser output performance among fluoride-based laser ceramics [67]. Nevertheless, further advancements are still necessary to enhance existing research outcomes and progress, particularly compared with other laser ceramic materials.

2 Fabrication of fluoride laser ceramics

2.1 Hot-forming technique

The hot-forming technique is a method of producing polycrystalline ceramics using high-purity single crystals as raw materials [110]. The single crystals are first heated to a temperature that transforms into a plastic state in a hot forging die and then subjected to uniaxial pressure to undergo plastic deformation. After crystallization and recrystallization, polycrystalline ceramics are produced [111]. The plastic deformation of single crystals leads to the formation of parallel dislocation arrays, which form domain walls and cellular structures [112]. Further deformation produces true grain boundaries, but the existing dislocation network still exists in the grains themselves [113]. Figure 3 shows schematic diagrams of the preparation of TCs by single-crystal hot forming and powder HP sintering [104]. The process of single-crystal hot forming is similar to that of powder HP sintering, and the optical quality of the ceramics after hot forging is equivalent to that of single crystals of

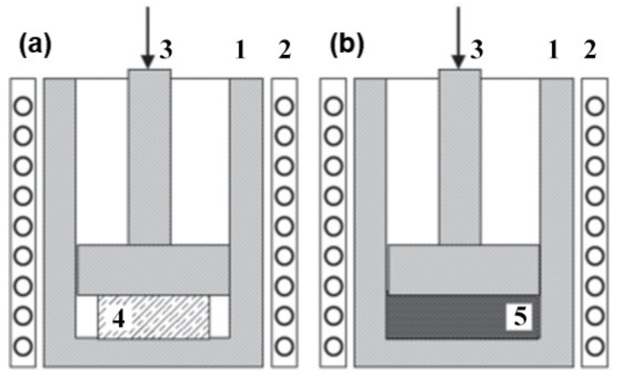

Fig. 3 Schematics of (a) hot-forming and (b) HP processes: (1) press die, (2) heater, (3) punch, (4) crystal, and (5) powders. Reproduced with permission from Ref. [104], © Pleiades Publishing, Ltd. 2021.

the same composition [30,114]. Moreover, owing to the destruction of the cleavage surface inside a single crystal during the preparation process, the mechanical properties of the ceramics produced are better than those of single crystals [107,114–118].

Basiev *et al.* explored the preparation of fluoride-based laser ceramics with high optical quality and performance comparable to those of single-crystal lasers through the hot forming technique and produced a series of Yb^{3+}-doped CaF_2–SrF_2–YbF_3 [105], Yb:CaF_2 [116], and Yb:BaF_2–SrF_2–CaF_3 [115] laser ceramics. Moreover, the laser performance of different rare earth ion-doped fluoride laser ceramics, such as Tm:CaF_2 [119–121], Er:CaF_2 [122,123], Pr:SrF_2 [106], and Nd:SrF_2 [101], prepared via the single-crystal hot forming method has been investigated. However, this method requires expensive single crystals as raw materials, and the optical quality of the ceramics produced is constrained by the single crystals, which requires that the single crystals should have high optical quality and be free of bubbles, cracks, stress, honeycomb-like substructures, and other growth defects [124]. Therefore, it greatly increases production costs and extends production cycles while discarding the advantages of ceramic gain media in the formation and preparation of different sizes and complex shapes.

To solve the high-cost problem of preparing fluoride-based laser ceramics via the hot forming method, the combination of powder preparation and ceramic sintering can significantly reduce the preparation cost while shortening the experimental cycle [17,20,125]. Therefore, more researchers are investigating the preparation of fluoride-based laser ceramics via the powder-forming sintering method.

2.2 Powder forming sintering method

The current mainstream preparation process for fluoride-based TCs is powder formation combined with ceramic sintering, which involves synthesizing high-quality powders, selecting appropriate molding processes to obtain green bodies with a certain strength, and finally sintering the green bodies to produce polycrystalline ceramics [14,15,92,126–128]. The synthesis of ideal powders has a decisive effect on the performance of subsequent ceramics. The particle size, particle size distribution, degree of agglomeration, and chemical purity of the powders significantly affect the densification process during sintering [129,130]. The appropriate particle size can obtain a greater sintering driving force during the sintering process; at the same time, the uniform and concentrated distribution of powder particles can ensure isotropic linear shrinkage of the powders in the early stage of sintering, and the relatively concentrated particle size distribution can also prevent differential shrinkage as much as possible, avoiding the uneven microstructure of the sample during sintering. The aggregation of powder particles causes uneven filling of the powders during the formation of the blank, and differential sintering can lead to the appearance of pores and microcracks inside the sintered samples [131]. Therefore, it is necessary to minimize the aggregation of powder particles as much as possible. The high purity of synthesized powders can reduce the probability of secondary phase formation or the introduction of impurity ions during sintering and reduce their absorption and scattering losses [23,132–135]. Table 2 summarizes the common powder synthesis approaches for fluoride TCs.

2.2.1 *Synthesis of powders*

The preparation of fluoride nanopowders by solid-state reactions involves the use of high-purity matrix raw materials such as CaF_2, BaF_2, and SrF_2 and rare earth fluoride raw materials such as YbF_3, TmF_3, and TbF_3 according to the designed stoichiometric ratio in a ball milling tank. After ball milling, mechanical crushing, uniform mixing, or wet mixing, the mixed powder slurry is dried, sieved, and green formed, and finally, reaction sintering is used to achieve the doping of target rare earth ions [22,67,136–139]. The Naoki team from Akita University in Japan successfully prepared Tm:BaF_2 [140] and Tb:BaF_2 [141] scintillation ceramics through a solid-phase reaction combined with spark plasma sintering (SPS). However, the optical quality of the fabricated ceramics was poor, and severe carburization occurred. The greatest advantages of the solid-phase reaction method are its simple process, high production efficiency, and ability to prepare ceramic powders in large quantities; at the same time, the disadvantage is also obvious. Impurities are easily introduced into powders during mechanical ball milling and crushing, making elimination difficult during subsequent screening and calcination processes. The introduction of impurities can cause absorption losses, seriously affecting the optical quality of ceramics.

At present, wet chemical methods are the most widely applied methods for synthesizing fluoride-based nanopowders internationally, including chemical coprecipitation methods [11,14,142–148], hydrothermal methods [149,150], and microemulsion micelle methods [108,151–154]. Chemical coprecipitation methods are highly favored by researchers because of their simple process, small particle size of synthesized powders, ability to achieve high concentration and uniform doping of rare earth ions, and low production cost [131]. The hydrothermal synthesis of powders was carried out in a closed container at high temperature and pressure. The synthesized powders have well-developed grains, a uniform particle size distribution, and a light degree of agglomeration. However, the hydrothermal method is limited by the instrument, and the output of the powders is low, so it is rarely used for the preparation of fluoride nanopowders. The preparation of nanopowders by the microlotion micelle method is caused by collisions between micelles. The prepared powders with controllable particle sizes, narrow particle size distributions, and minimal agglomeration, are not limited by instruments and have strong operability. However, this method consumes a large amount of surfactants and organic solvents during the preparation process, which easily adsorb on the surfaces of particles to form impurities. Moreover, the sintering temperature of fluoride ceramics is lower than that of oxides, making it difficult to fully eliminate them at lower calcination temperatures, which can lead to deterioration of the optical quality of the produced ceramics [155].

2.2.2 *Compaction of green bodies*

After high-quality fluoride ceramic powders are synthesized, appropriate molding processes are selected to obtain fluoride ceramic blanks with uniform structures and high densities. The mainstream process used to form fluoride-based ceramic powders internationally is dry pressing combined with cold isostatic pressing (CIP). Dry pressing is a simple operation that applies uniaxial pressure to a certain mass of powders placed in a specific mold to form a green body with a specific shape. This method can achieve rapid pressing of large quantities of ceramic blanks. However, during the dry pressing process, the stress on the pellets in the axial and radial directions is inconsistent, which can lead to uneven internal structures of the blanks, and in severe cases, peeling may occur. Therefore, after dry pressing, the blanks are often subjected to CIP to ensure the uniformity of the internal structure of the blanks and further increase the density of the ceramic bodies. CIP is the process of placing samples in a liquid medium after vacuum sealing and using the liquid medium to apply pressure evenly to the surfaces of the pellets. The blanks are subjected to uniform isotropic stress. Li's group from the Shanghai Institute of Ceramics, Chinese Academy of Sciences, successfully prepared a series of Yb:CaF_2 [127,183], Yb, La:CaF_2 [184], Er:CaF_2 [128], and Er:SrF_2 [142] fluoride laser TCs by

Table 2 Common powder synthesis approaches for fluoride transparent ceramics

Ceramic	Approach	Ref.
CaF_2 based ceramic	Solid phase reaction	[67,108,136–138]
	Coprecipitation	[11,15,23,108,109,127,128,132,135,137,142,147,148,156–192]
	Hydrothermal method	[149,150]
	Microemulsion micelle	[108,151,152]
SrF_2 based ceramic	Solid phase reaction	[193,194]
	Coprecipitation	[14,22,133,134,139,142,147,179,180,186,195–217]
BaF_2 based ceramic	Coprecipitation	[126,129,143,144,218–220]

subsequent sintering of the green bodies formed by dry pressing and CIP. Luo *et al.* [219,220] from Nanchang Hangkong University synthesized Ce:BaF_2 precursors through a chemical coprecipitation method. Ce:BaF_2 TCs were fabricated via vacuum sintering after dry pressing combined with CIP. The preparation of BaF_2-based TCs is difficult, and related research started relatively late. Currently, the mainstream methods for preparing BaF_2-based TCs are HP sintering and cold sintering processes (CSP) [21,221,222].

2.2.3 *Ceramic sintering*

After synthesizing high-quality nanopowders and obtaining ceramic green bodies with a certain strength and density through dry pressing and CIP, it is necessary to select an appropriate sintering process to ensure that the green bodies gradually densify and that pores are discharged during the sintering process to obtain TCs with high density, low porosity, and a uniform structure. Researchers of fluoride-based TCs have adopted sintering techniques such as vacuum HP sintering [15,68,144,195,223,224], CSP [147,148,188,225], HIP sintering [11,142,184,189], vacuum sintering [127,220], and SPS [166,226,227].

Table 3 shows the main compaction methods used for fluoride TC fabrication.

HP sintering was the earliest and most widely used sintering process in the field of fluoride-based TCs. Figure 4 shows a schematic diagram of fluoride ceramics produced by HP sintering of powders synthesized via the coprecipitation method. HP specifically refers to placing the powders in a specific mold while heating and applying uniaxial pressure. The applications of pressure intensifies the mass transfer and diffusion behavior between powder particles, greatly reducing the sintering temperature and shortening the sintering time of ceramics, which is conducive to obtaining ceramics with fine grains and excellent

Table 3 Main compaction methods for fluoride transparent ceramic fabrication

Ceramic	Method	Ref.
CaF_2 based ceramic	Hot forming	[105–107,111,115,116,118–120,122,123,240,265,266]
	HP sintering	[11,109,116,117,127,132,135,137,138,145,146,156,158–165,167,169,170,172–178,180–182,185,186,190,191,195,196,198,208,210,224,228–240,267–271]
	CSP	[148,188]
	HIP	[11,67,128,142,183,184,189,192,272,273]
	Vacuum pressureless sintering	[109,127,168,183,224,228,272]
	SPS	[166,226,227,249–257,263,264]
SrF_2 based ceramic	Hot forming	[101,106,110,201,274,275]
	HP sintering	[14,22,134,139,179,180,186,194–196,198,200–203,207–212,214–216,241]
	SPS	[258–260]
BaF_2 based ceramic	HP sintering	[126,129,144,204,206,218,223,242,244]
	SPS	[140,141,221]
	Vacuum pressureless sintering	[143,219,220]
	CSP	[21,225]

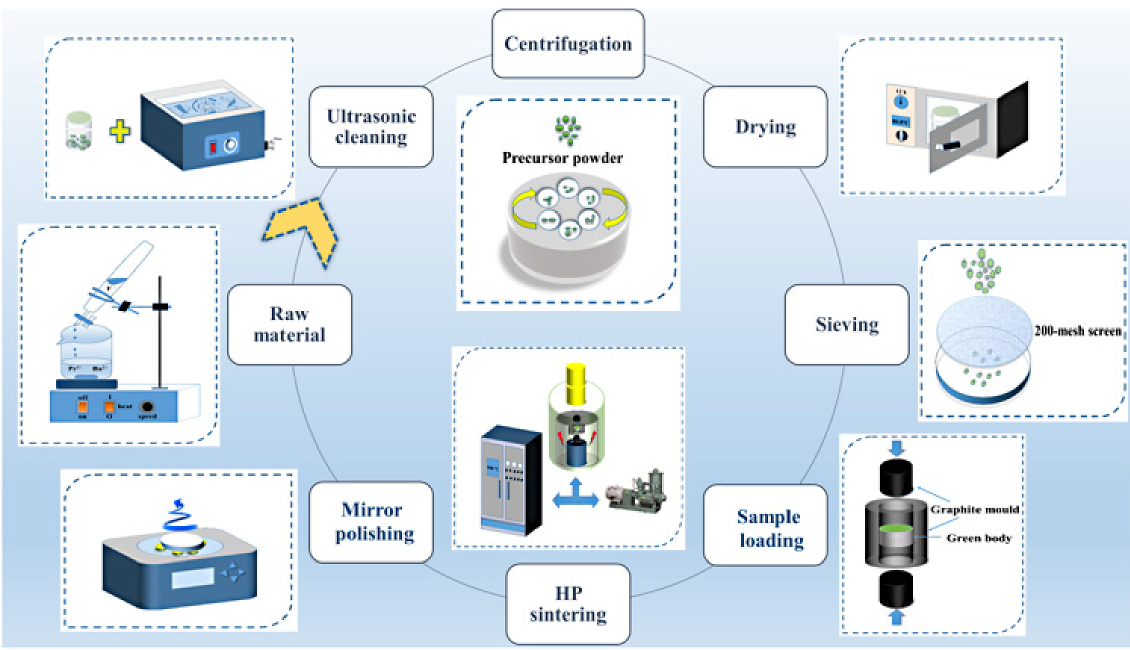

Fig. 4 Schematic diagram of fluoride ceramics produced by HP sintering of powders synthesized via coprecipitation method. Reproduced with permission from Ref. [126], © Elsevier B.V. 2021.

mechanical properties [104]. A schematic diagram of its structure is shown in Fig. 3(b) [104]. Since the first Dy:CaF_2 [68] laser ceramics obtained by HP in 1964, many researchers have been involved in the preparation of fluoride-based TCs through HP sintering. At present, Yb:CaF_2 [228,229], Nd:CaF_2 [230,231], Er:CaF_2 [232–237], Ho:CaF_2 [238,239], Eu:CaF_2 [240], Nd:SrF_2 [215], Yb:SrF_2 [241], Er:SrF_2 [186,208,212,214], BaF_2 [223,242], Pr:BaF_2 [126,129], Ce:BaF_2 [144,243,244], and other rare earth ion-doped fluoride-based TCs have been prepared via HP sintering.

CSP is an emerging sintering process that has emerged in recent years. By adding an appropriate amount of liquid phase (water or volatile solvent) to the powder particles, the powder particles are uniformly wetted, and high pressure (200–900 MPa) is applied while the powders are heated at low temperature. This can effectively enhance the mass transfer and diffusion behavior between particles, ultimately achieving the preparation of ceramics far below the sintering temperature (100–900 °C) in a short time [245,246]. CSP can be described at the macro- and microlevels, as depicted in Fig. 5 [245]. CSP can greatly reduce production costs, and the operation is simple and controllable, and a lower sintering temperature and high pressure can also suppress abnormal grain growth [148,247]. Liu's group from Hangzhou Dianzi University took the lead in applying cold sintering technology to the preparation of fluoride ceramics and successfully prepared BaF_2 [21,225] and LiF [247] TCs with commercial raw powders. Gao *et al.* [148] from Donghua University successfully prepared Yb:CaF_2 TCs via CSP technology at low temperatures and high pressures of only 350 °C and 500 MPa. Guo *et al.* [147,188] from Guilin University used precursor powders synthesized via the coprecipitation method to fabricate CaF_2 and Er:SrF_2 TCs via the CSP method. However, ceramics prepared by CSP have insufficient grain development and amorphous phase pinning in the grain boundary area, which usually requires annealing at a certain temperature [246].

HIP sintering has been a highly favored sintering process in the field of TCs in recent years. By applying uniform pressure to a presintering ceramic sample while it is heated, the sintering driving force provided by high temperature and high pressure can further discharge the internal pores of presintering ceramics, greatly improving their optical quality [17,20,131]. The sintering method of powder compaction and ceramic presintering, combined with HIP posttreatment, has become the mainstream process for the large-scale preparation of high-quality, complex-shaped TCs. In 2017, Kitajima *et al.* [67] successfully prepared Yb:CaF_2–LaF_3 laser ceramics through air presintering combined with HIP, achieving a laser output with a slope efficiency of up to

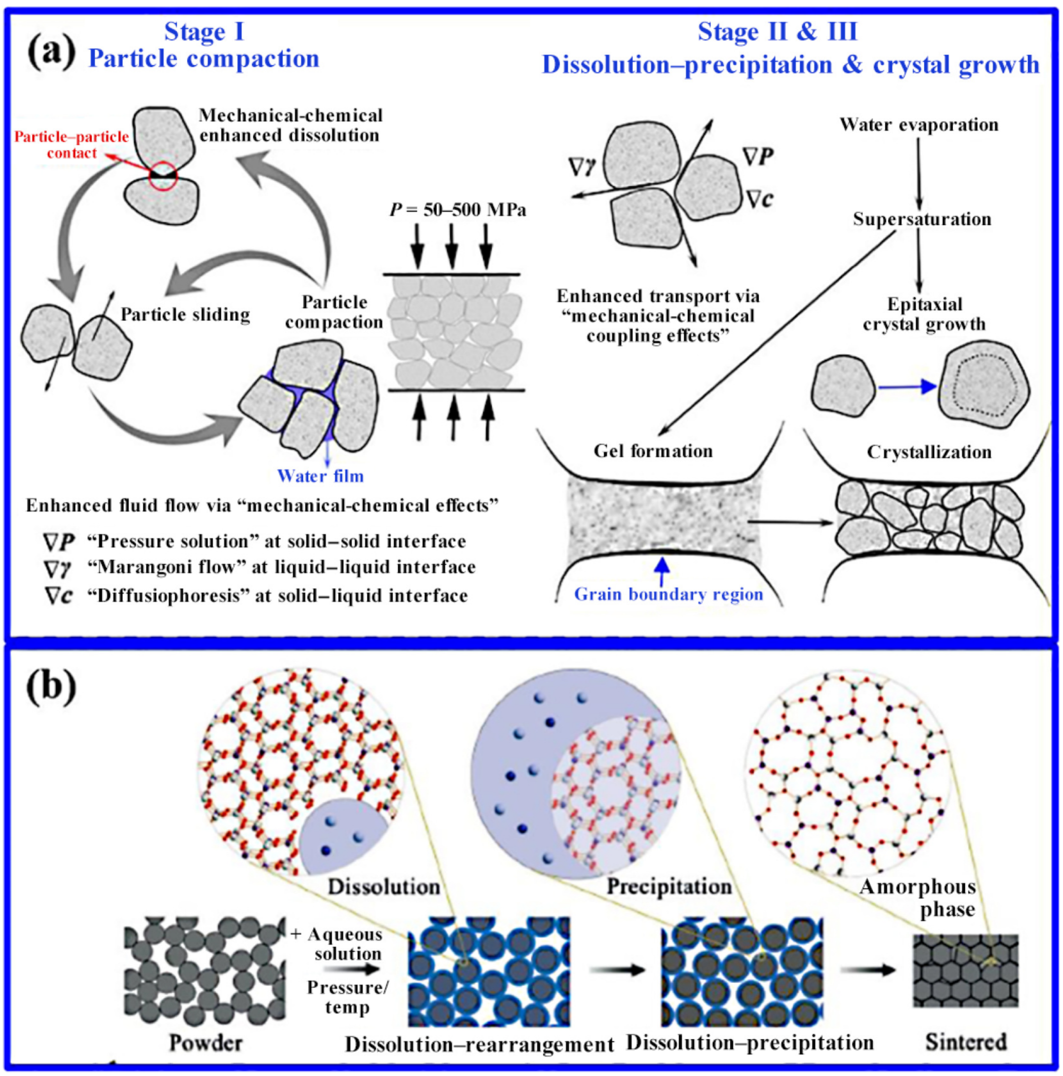

Fig. 5 Principles and process of cold sintering: (a) three stages of CSP and (b) mechanism of cold sintering at microstructure level. Reproduced with permission from Ref. [245], © Elsevier B.V. 2018.

69.5%. Guo *et al.* [11] optimized the optical quality of $Yb:CaF_2$ laser ceramics through a two-step sintering process of HP combined with HIP posttreatment in 2023. They obtained a quasicontinuous wave (QCW) laser output with an output power of 1.12 W and a slope efficiency of 11.6% in subsequent laser tests.

Vacuum pressureless sintering facilitates the elimination of pores and densification of ceramic blanks during sintering by placing them in a high vacuum environment, thereby achieving the transparency of ceramics [248]. However, unlike HP and CSP, which involve pressure-assisted sintering to provide a driving force, vacuum pressureless sintering generally requires a longer insulation time and higher sintering temperature to ensure full elimination of pores, which undoubtedly increases production costs. Therefore, after vacuum pressureless sintering, the blank is usually combined with HP or HIP posttreatment to further improve its optical quality. Li's group [127,183] from the Shanghai Institute of Ceramics, Chinese Academy of Sciences, prepared $Yb:CaF_2$ laser ceramics by vacuum presintering combined with HP posttreatment and HIP posttreatment. Li *et al.* [143] from Hainan University prepared $Nd:BaF_2$ TCs through long-term vacuum sintering for 10 h, with an average grain size of 420 μm.

SPS utilizes the thermal effect generated by the direct current pulse. The current passes through the mold to heat the sample, and pressure is applied during the heating process to achieve ceramic sintering. The heating rate of SPS can reach 1000 °C/min, and the most prominent features of SPS are its extremely short insulation time, lower sintering temperature, and small grain sizes. The Naoki team from Akita University successfully prepared CaF_2 [249,250], $Nd:CaF_2$ [226], $Eu:CaF_2$ [251], $Dy:CaF_2$ [252], $Ce:CaF_2$ [253], $Na:CaF_2$ [254], $Mn:CaF_2$ [255,256], $Li:CaF_2$ [257], SrF_2 [258], $Eu:SrF_2$ [259], $Tb:SrF_2$ [260], BaF_2 [221], $Tm:BaF_2$ [140], $Tb:BaF_2$ [141], $Ce:MgF_2$ [261], and $Gd:MgF_2$ [262] TCs via SPS with commercial powder mixtures. However, the optical quality of the fabricated ceramics was poor, and there was carbon contamination inside the ceramics. Li *et al.* [166] from Wuhan University of Technology prepared $Yb:CaF_2$ TCs via SPS at a low sintering temperature of 600 °C, obtaining an average grain size of only 130 nm. However, SPS also has fatal drawbacks. Owing to the use of graphite molds, carbon impurities are easily introduced during the sintering process, and the sizes and shapes of the prepared samples are limited by the molds, making large-scale production of ceramic samples impossible [263,264].

3 Fluoride laser ceramics

3.1 Visible light band rare earth ion-doped fluoride laser ceramics

The visible light spectrum (380–780 nm) serves as a crucial domain for laser applications across various fields, such as information storage, laser displays, laser medicine, and underwater optical communication [146,190,211]. The activated ions that can achieve visible laser output include Pr^{3+}, Dy^{3+}, and Tb^{3+} [190] and Sm^{3+}, Ho^{3+}, Er^{3+}, and Eu^{3+} [149,170,240]. Among them, Pr^{3+} and Dy^{3+} have been extensively studied, as their absorption peaks are in the blue light band and can be pumped by a blue light laser diode (LD). The Pr^{3+} emission band covers blue, green, orange, and red light, whereas the Dy^{3+} emission band is yellow light, which basically covers the entire visible band [9].

3.1.1 Pr^{3+}-doped fluoride laser ceramics

In 2011, Basiev *et al.* [106] prepared $Pr^{3+}:SrF_2$ (0.3 and 0.5 at%) ceramics via single-crystal hot forming technology. For the first time, a laser in the visible spectral range (639 nm) was obtained under GaInN blue laser diode optical pumping, and they successfully achieved continuous wave (CW) operation with a lasing threshold of less than 100 mW of absorbed pump power, accompanied by a slope efficiency exceeding 9%. Optical materials doped with Pr^{3+} ions face limitations arising from the pronounced concentration quenching effect among Pr^{3+} ions at high doping concentrations, leading to a rapid decline in the luminescence intensities of fluoride-based materials [209]. Pr^{3+} ions within fluoride crystal lattices tend to aggregate into clusters, exacerbating emission intensity quenching, even at low doping concentrations of Pr^{3+} ions [178]. To mitigate this concentration quenching effect, various codopants, such as Gd^{3+}, Y^{3+}, and La^{3+}, can be introduced as sensitizer ions into matrix materials doped with Pr^{3+} ions. The incorporation of these buffer ions into fluorite optical materials results in the formation of new emission centers [M^{3+}–Re^{3+}] and the dispersion of [Pr^{3+}–Pr^{3+}] clusters, thereby enhancing the luminescence properties and mitigating the extent of emission intensity quenching [276]. Moreover, the introduction of trivalent nonactive buffer ions into fluoride crystal lattices can alter the charge balance of the fluorite substrates, thereby modifying the microstructures and optical transparency of the final ceramics.

Since 2019, Yi *et al.* have fabricated (0.2, 0.5, 1.0, 1.5, 3.0, and 5.0 at%) $Pr:CaF_2$ [178], 1.0 mol% $Pr:(Ca_{0.97}Gd_{0.03})F_{2.03}$ [271], (0.2, 0.5, 1.0, and 2.0 at%) Pr, 6 at% $Gd:SrF_2$ [202], and 1 at% Pr, (0, 1, 3, 6, 10, and 15 at%) $Gd:CaF_2$ [146] ceramics through HP. Ceramics were fabricated by synthesizing precursor powders through chemical coprecipitation, followed by two steps (400 °C, calcination for 2 h; 800 °C, 40 MPa, sintering for 1.5 h). The in-line transmittance of the 2 mm thick samples at 1200 nm ranged from 86%–90%. With increasing Pr^{3+} doping concentration, the emission intensity and decay lifetime generally decrease because of the concentration quenching effect [178]. However, with the codoping of Gd^{3+} ions, the emission characteristics significantly increased because of the mitigation of the concentration quenching effects [146]. Through Gd^{3+} codoping, the emission intensity at 642 nm associated with the $3P_0 \rightarrow 3F_2$ transition increased by up to 50-fold, attributed to alterations in the coordination environment that led to an increase in the quenching threshold of Pr^{3+} ions (Fig. 6). Liu *et al.* [22, 139, 209] from Xinyang Normal University first synthesized SrF_2 powders via the chemical coprecipitation method and then mixed the

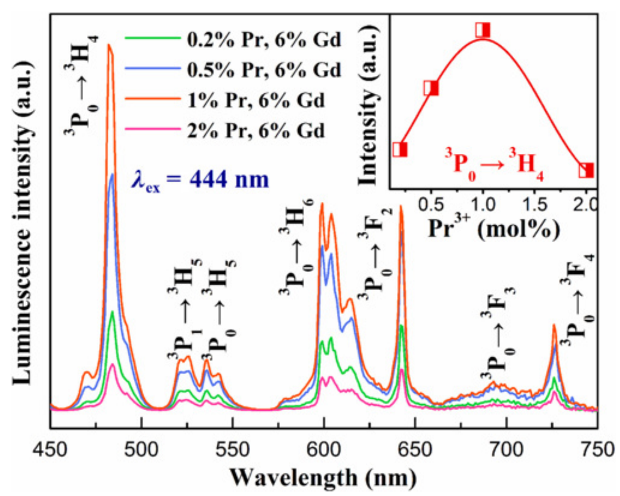

Fig. 6 Fluorescence spectra of $Pr:Ca_{0.94}Gd_{0.06}F_{2.06}$ TCs with different Pr^{3+} contents excited by a 444 nm xenon lamp. Inset shows dependence of Pr^{3+} concentration on luminescence intensity at 483 nm. Reproduced with permission from Ref. [146], © Elsevier Ltd. and Techna Group S.r.l. 2022.

synthesized SrF_2 powders with commercial PrF_3, LaF_3, and YbF_3 powders via ball milling in anhydrous alcohol. Finally, (0.1, 0.5, 1, 3, 5, and 10 wt%) Pr:SrF_2 [209], 3 wt% Pr, (0, 0.5, 1, 3, 5, and 10 wt%) La:SrF_2 [139], and 3 wt% Pr, (0, 2, 5, 7, 10, and 15 wt%) Yb:SrF_2 [22] ceramics were successfully fabricated through HP. The highest transmittances of the 2 mm thick Pr:SrF_2 ceramics at 350 and 1200 nm were 90.4% and 91.9%, respectively. The luminescence intensities of Pr,La:SrF_2 and Pr,Yb:SrF_2 ceramics were drastically enhanced through LaF_3 and YbF_3 codoping.

In 2021, Liu *et al.* [126,129] of Wuhan University of Technology synthesized 5 at% Pr:BaF_2 ceramics with high optical quality and (0, 0.5, 1, 2, 3, and 5 at%) Pr:BaF_2 ceramics with different Pr^{3+} concentrations via HP. As the concentration of Pr^{3+} increased, the emission spectrum and fluorescence decay time increased, followed by a decrease, culminating in a peak value of 261 ns at 0.5 at%, which was attributed to the cross-relaxation phenomenon between Pr^{3+} ions.

3.1.2 Dy^{2+}-doped fluoride laser ceramics

In 1964, the first laser ceramic Dy^{2+}:CaF_2 was prepared by Hatch *et al.* [68] through HP, and laser output was achieved at liquid helium temperature, officially marking the beginning of the development of laser ceramics for solid-state lasers. In 2021, Mei's group [211,237] chose HP to fabricate (1, 2, 3, 4, and 5 at%) Er^{3+}, 3 at% Dy^{3+}:CaF_2, and (0.5, 1, 3, 5, 7, and 9 mol%) Dy:SrF_2 TCs with precursor powders synthesized via the chemical coprecipitation method. The emission intensity initially increased and subsequently decreased with increasing Dy^{3+} doping concentration upon excitation at 349 nm, peaking at 1.0 mol% doping (Fig. 7). The quenching threshold for Dy:SrF_2 TCs was determined to be between 0.5 and 3.0 mol%, with an analysis conducted on cross relaxation mechanisms among Dy^{3+} ions as the primary cause of concentration quenching. On the basis of CIE chromaticity coordinates, Dy:SrF_2 TCs demonstrated the ability to generate white light emission, with SrF_2 ceramics doped with a 7.0 mol% concentration of Dy^{3+} ions exhibiting the closest approximation to perfect white light. These findings underscore the potential of Dy:SrF_2 TCs as promising candidates for solid-state laser materials operating within the visible spectrum.

3.2 1 μm band rare earth ion-doped fluoride laser ceramics

Lasers with a 1 μm band are widely used in industrial processing, remote sensing, medical treatment, frequency doubling light sources, human eye safety, and other fields [49,182]. The rare earth ions that can be used to obtain lasers in this band are mainly Yb^{3+} and Nd^{3+}, which have been extensively studied. Among all rare-earth ions, Yb^{3+} stands out as particularly attractive because of its simple electronic structure, lack of intrinsic processes for concentration quenching, long lifetime, and broad emission spectra [277–279]. These unique characteristics render Yb^{3+} highly suitable for applications in ultrashort and high-power lasers. Similarly, within the lanthanide rare-earth ion family, Nd^{3+} is renowned for its precise operation as a four-level laser system characterized by low pump thresholds and its efficient energy

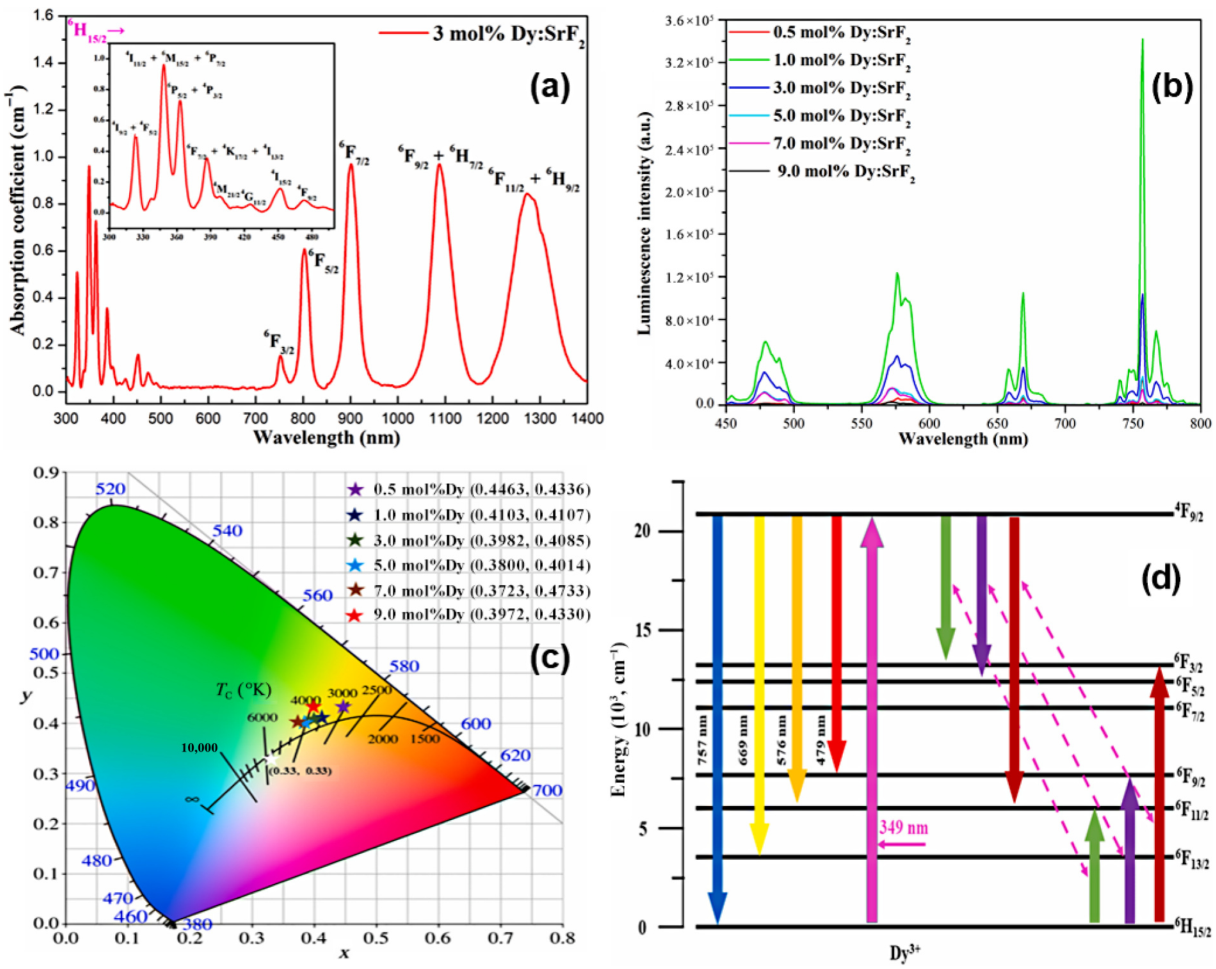

Fig. 7 (a) Absorption spectra, (b) emission spectra, (c) CIE chromaticity coordinates of Dy:SrF_2 TCs with different Dy^{3+} doping concentrations, and (d) schematic energy level diagram of Dy^{3+} together with possible cross relaxation processes in Dy:SrF_2 ceramics. Reproduced with permission from Ref. [211], © Elsevier B.V. 2021.

storage and extraction capabilities. Furthermore, the unique absorbance distribution of Nd^{3+} facilitates the utilization of commercially available laser diodes as pumping sources. These inherent advantages position Nd^{3+} as a highly significant ion in the technical advancement of next-generation, all-solid-state ultrashort, and high-power lasers [101,230].

3.2.1 Yb^{3+}-doped fluoride laser ceramics

In 2008, Basiev *et al.* [105] successfully fabricated high-quality CaF_2–SrF_2–YbF_3 TCs through the hot forging single-crystal method, marking the first instance of achieving laser output from such materials. The ceramic sample demonstrated a laser slope efficiency of 45%, which was merely 5% lower than that of CaF_2–SrF_2–YbF_3 crystals produced by the crucible descent method at the time (Fig. 2). Notably, the ceramics exhibited a superior laser damage threshold and higher fracture toughness than its single-crystal counterparts. The next year, Basiev *et al.* [115] compared the physicochemical and oscillation properties of CaF_2:Yb (3%) crystals and CaF_2:Yb (5%) ceramics fabricated via hot forming. In 2009, Abury *et al.* [108] synthesized Yb:CaF_2 nanopowders via mechanical mixing, the reverse micelle method, and the coprecipitation method. They conducted a comparative analysis of the particle size distribution among the three powder types and investigated the impact of annealing treatment on the infrared spectrum of powders generated via the coprecipitation method. The powders derived from the coprecipitation method were subsequently chosen for ceramic sintering to fabricate 10 at% Yb:CaF_2 TCs. However, the resulting ceramics exhibited suboptimal optical quality, with an in-line transmittance of only 55% for the 1 mm thick samples at 1200 nm.

In 2011, Lyberis *et al.* [109,191] synthesized Yb:CaF_2 nanopowders via the coprecipitation method and then employed vacuum presintering in conjunction with HP to fabricate 0–10 at% Yb:CaF_2 TCs. The optimal composition to achieve the best transparency was close to 5 at% ytterbium-doped CaF_2. The optical losses of the samples were minimal, measuring 0.16 cm^{-1} at 1200 nm; however, they are not yet sufficient to achieve an efficient laser effect. Experimental tests revealed that these losses stem from defects localized at the grain boundaries. Two distinct defect types have been discerned: ytterbium segregation and the presence of an oxygenized secondary phase, with the latter being the primary source of scattering. Specifically, the discrepancy in refractive between the pure calcium oxide secondary phase (1.871) and calcium fluoride (1.434) resulted in a reflectance of 1.6% and could induce an absorption band at 220 nm (Yb–O charge transfer band). Furthermore, this study revealed that the synthesized particles were enveloped by an oxygenized shell with nonuniform thickness across individual particles (Fig. 8). Subsequently, they modified the synthesis protocol to tentatively improve the quality of the ceramics by suppressing this shell and successfully fabricated 0.1, 1, 5, and 10 at% Yb:CaF_2 ceramics [224]. They investigated the effect of Yb^{3+} ions doping concentration on fluorescence lifetime, absorption, emission spectra of Yb:CaF_2 ceramics, and the existence form of Yb^{3+} in the matrix lattice, as well as the spectra and energy levels of Yb^{3+} ions in CaF_2 TCs [228]. 1 at% Yb:CaF_2 ceramic sample had successfully demonstrated laser gain in an Ω-shaped cavity, and the output was not affected by pump wavelength changes from 973 to 979 nm.

Akchurin *et al.* [116] fabricated Yb:CaF_2 TCs via the hot forming method and HP sintering and compared their optical,

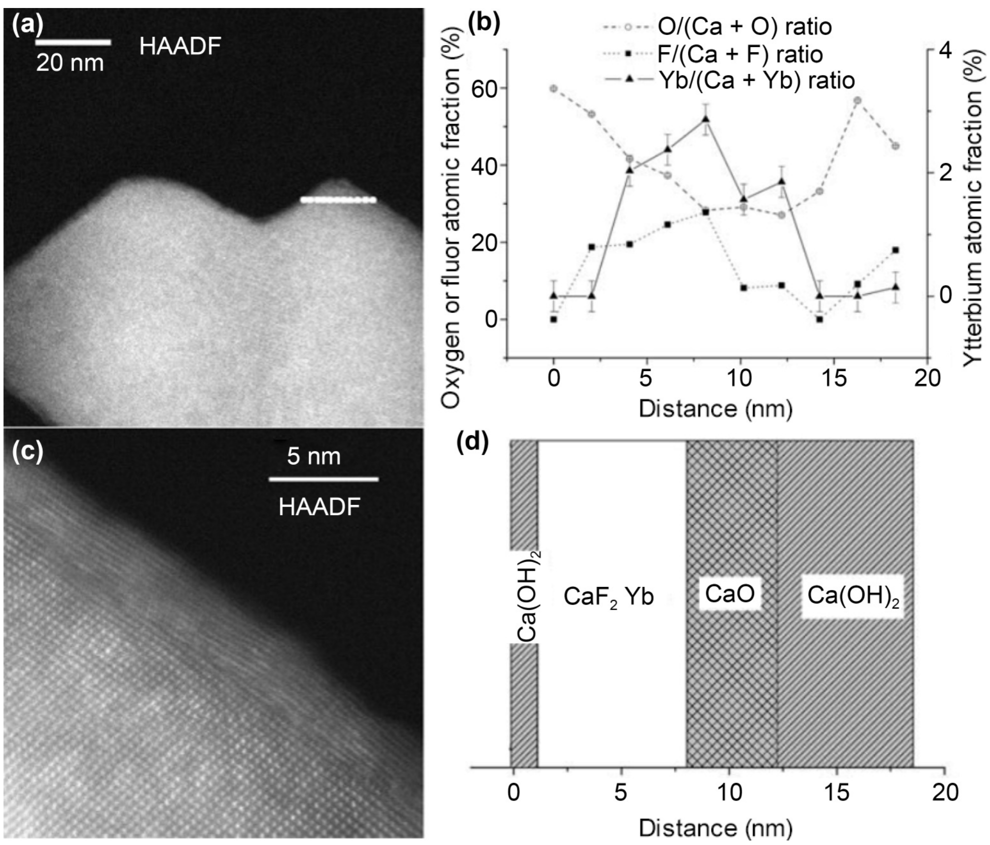

Fig. 8 (a) HAADF-STEM image of a 5 at% Yb:CaF_2 powder particle with EDX analysis of shell composition. (b) EDX profile with Yb/(Yb+Ca) ratio (solid line), O/(O+Ca) ratio (dashed line), and F/(F+Ca) ratio (dotted line). (c) HAADF-STEM image of shell of same particle, and (d) schematic view of composition along this profile. Reproduced with permission from Ref. [191], © Elsevier Ltd. 2011.

thermal, and mechanical properties with those of $Yb:CaF_2$ single crystals in 2013. The findings revealed that $Yb:CaF_2$ ceramics exhibited thermal conductivity comparable to that of single crystals, and the microhardness, fracture toughness, and continuous laser output performance of ceramics prepared via the hot forming method matched those of single crystals. $Yb:CaF_2$ TCs produced by HP powder sintering exhibited superior mechanical properties and achieved laser output for the first time. In the same year, Shirakawa *et al.* [280] fabricated ytterbium-doped CaF_2–LaF_3 TCs from nanocrystals. 3% Yb^{3+}-doped ceramics displayed broadband absorption and fluorescence spectra akin to those of $Yb^{3+}:CaF_2$ crystal. The laser operation yielded an output power of 1.09 W with a slope efficiency of 35%. In 2015, Aballea *et al.* [281] synthesized $Yb:CaF_2$ powders via the coprecipitation method combined with a special strain-free mode and pressureless air sintering, successfully preparing 4 at% $Yb:CaF_2$ TCs with high optical quality. This method eliminates the need for pressure-assisted sintering and results in ceramics demonstrating continuous laser output with a slope efficiency of 43% and a maximum power of 1.6 W in laser performance testing. Indeed, both the transmission spectra and laser properties were improved compared with those of ceramics fabricated via conventional methods [168]. In 2017, the same group investigated the thermal conductivity of 1.5–5 at% $Yb:CaF_2$ TCs via the 3*w* method, a technique used to measure the thermal conductivity of materials by analyzing the electrical response of a specially designed transducer applied to the sample [282]. The results obtained for the doped samples closely resembled those for $Yb:CaF_2$ single crystals with equivalent doping levels, indicating a significant enhancement in thermal properties of TCs. The fitting parameters suggested that the incorporation of a doping element into the lattice had a greater influence on the thermal conductivity than did the presence of grain boundaries in the materials. Since 2016, Kitajima *et al.* [67,283] uniformly mixed YbF_3, LaF_3, and CaF_2 nanopowders via the wet method, formed a green body through dry pressing and CIP processes, and successfully prepared $Yb:CaF_2$–LaF_3 TCs via air presintering and HIP posttreatment. They achieved CW laser operation with a maximum output of 3.97 W, accompanied by a remarkable maximum slope efficiency of 73.1% [283]. In subsequent laser experiments, TCs with 3 at% La and 1 at% Yb achieved an optimal slope efficiency of 69.5%, whereas those with 3 at% La and 2 at% Yb reached a maximum output power of 4.36 W [67]. This is currently the highest laser output for calcium fluoride laser ceramics (Fig. 9).

Using the SPS method, Li *et al.* [166] prepared 5 at% $Yb:CaF_2$ ceramics with a mean grain size of approximately 130 nm through precursor powders synthesized via the chemical coprecipitation method. The transmittance of 2 mm thick sample at 1200 nm was 83%, which was lower than the 90% transmittance of hot-pressed sintered sample. Moreover, the fluorescence lifetime and emission spectra of Yb^{3+} at different wavelengths were obtained. On this basis, Li *et al.* [181] investigated the effects of Yb^{3+} doping concentration on the microstructure, spectrum properties, and laser performance of $Yb:CaF_2$ laser ceramics through HP. The maximum doping concentration of Yb ions in CaF_2 was approximately 25 at%. The in-line transmittance of all ceramics, each 3.5 mm thick, reached 90% at 1200 nm. Nonetheless, this value decreased as the wavelength decreased. As the concentration of Yb ions increased, both the particle size of the powders and the grain size of the ceramics decreased (Fig. 10), whereas the bandwidths of the emission peaks gradually expanded. The use of 5 at% $Yb:CaF_2$ as the gain medium yielded a maximum output power of 0.809 W, with the slope efficiency and optical-to-optical efficiency reaching 19.6% and 12.18%, respectively [181]. These authors subsequently investigated the laser characteristics of $Yb:CaF_2$ laser ceramics. By utilizing a semiconductor saturable absorber mirror devoid of supplementary dispersion compensation elements, a continuous-wave mode-locked laser achieved a pulse duration as short as 575 fs, operating at a central wavelength of 1048.5 nm [284].

Despite great achievements in achieving excellent laser performance with $Yb:CaF_2$ [116,281] and $Yb:CaF_2$–LaF_3 [67,280,283] TCs, there remains a significant challenge due to the high scattering coefficient at short wavelengths, which currently

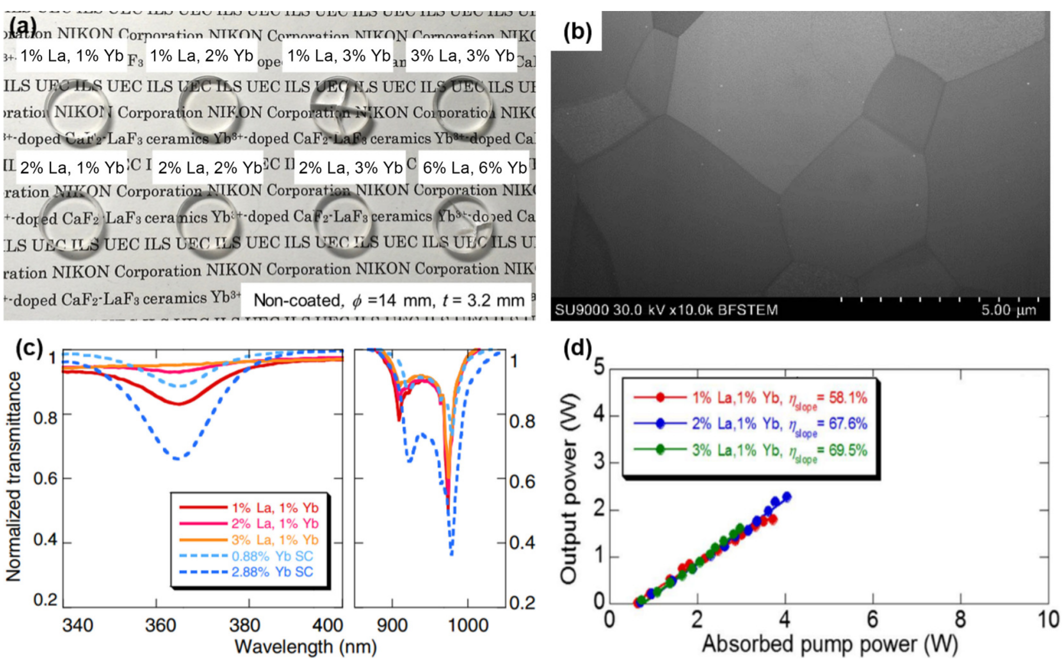

Fig. 9 (a) Photograph of $Yb:CaF_2$–LaF_3 ceramics, (b) SEM image of 3 at% Yb-doped CaF_2–LaF_3 ceramics, (c) absorption spectra of $Yb:CaF_2$–LaF_3 ceramics and $Yb:CaF_2$ single crystals, and (d) output power of 1 at% $Yb:CaF_2$–LaF_3 ceramic laser vs. absorbed pump power. Reproduced with permission from Ref. [67], © Optical Society of America 2017.

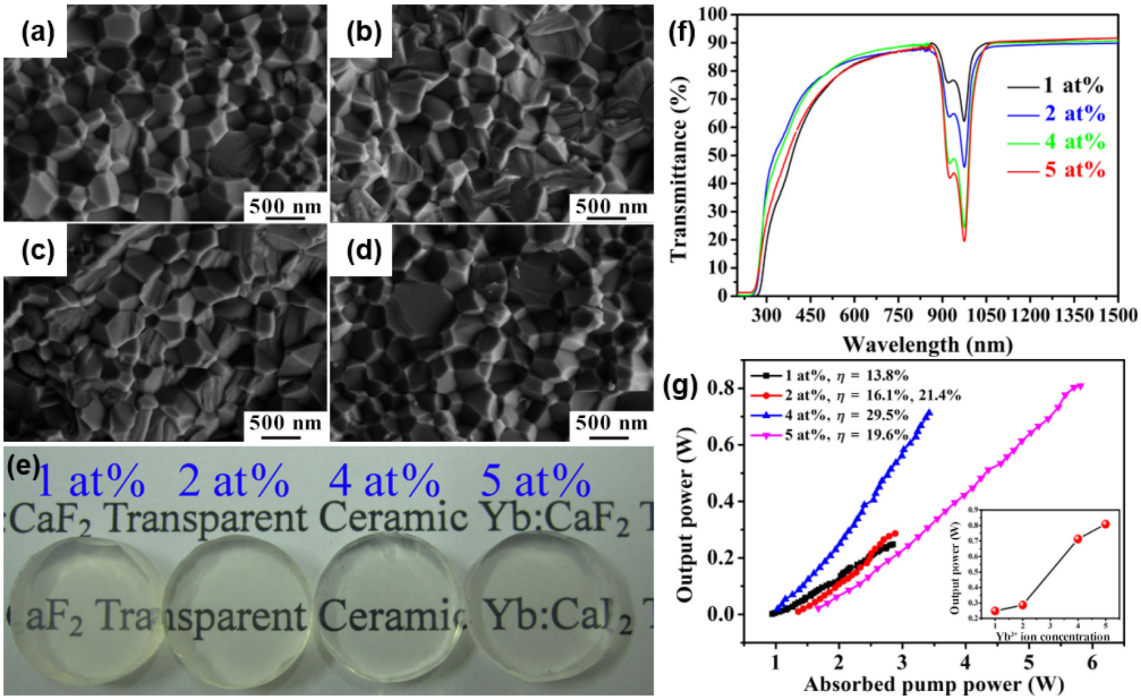

Fig. 10 SEM micrographs of $Ca_{1-x}Yb_xF_{2+x}$ ceramic fracture surfaces: (a) $x = 0.01$, (b) $x = 0.02$, (c) $x = 0.04$, and (d) $x = 0.05$. (e) Photograph and (f) in-line transmittance of Yb:CaF_2 ceramic samples with different Yb^{3+} doping concentrations and (g) CW output power vs. absorbed pump power for ceramic samples with different Yb^{3+} doping concentrations, representing slope efficiency. Reproduced with permission from Ref. [181], © The American Ceramic Society 2020.

limits laser output power. Enhancing transmittance in the visible range is the primary challenge. Given the successful fabrication of yttrium aluminum garnet (YAG) laser ceramics utilizing SiO_2 as a sintering aid [285], investigating the impact of sintering aids on the fabrication of fluoride TCs is of considerable interest. Hence, buffer ions (i.e., Na^+, Y^{3+}, La^{3+}, and Gd^{3+} ions) have been introduced into fluoride TCs to manipulate their spectroscopic properties. Li *et al.* [137] fabricated 5 at% Yb:CaF_2 TCs with different concentrations of NaF through HP. The presence of NaF served dual purposes in the Yb:CaF_2 ceramics. First, as a sintering aid, NaF impedes grain growth and notably enhances the transmittance in the visible region. The transmittance levels in 1 mm thick NaF-doped samples reached 83% and 85% at wavelengths of 400 and 1200 nm, respectively (Fig. 11). Second, NaF doping prevented the formation of Yb^{3+} ion clusters within Yb:CaF_2 ceramics. This resulted in increased emission intensity at 1028 nm and prolonged luminescence lifetimes with increasing NaF doping concentrations. In addition, Li *et al.* [182] further investigated the influence of Y^{3+} ion doping on the spectroscopic properties of 3 at% Yb:CaF_2 TCs. As the concentration of Y^{3+} ions increased, the particle size of Yb:CaF_2 powders decreased, whereas the emission intensity at 1028 nm and lifetime initially increased before decreasing. CW laser emission at a wavelength of 1049 nm was achieved in 3 at% Yb, 1 at% Y:CaF_2 ceramics, reaching a maximum output power of 1.16 W with a slope efficiency of 29.3% [182]. In 2022, Liu *et al.* [229] tested the pulse laser output performance of calcium fluoride ceramics for the first time using Yb,Y:CaF_2 TCs provided by Wuhan University of Technology. The pulse width was 8.9 ps, and the repetition frequency was 0.23 THz (Fig. 12).

Since 2019, Wei *et al.* [127,183,184,189] have utilized a two-step sintering method for the preparation of Yb:CaF_2 laser ceramics. Their research investigated the impact of the sintering temperature, doping ion concentration, and codopants on the microstructure and laser performance of Yb:CaF_2 laser ceramics. Wei *et al.* [127] successfully prepared 5 at% Yb:CaF_2 TCs via vacuum presintering in conjunction with HP posttreatment from coprecipitated powders, achieving a maximum output power of 0.9 W with a notable slope efficiency of 23.6% in laser testing. The in-line transmittance of 1.5 mm thick Yb:CaF_2 TCs, which were fabricated through presintering at 600 °C for 1 h followed by HP posttreatment at 700 °C for 2 h, reached 92.0% at 1200 nm. The sample exhibited a homogeneous microstructure with an average grain size of 360 nm. Using the two-step sintering method of vacuum sintering combined with HIP posttreatment, Liu *et al.* [183] produced 5 at% Yb:CaF_2 TCs, 3 mm in thickness, presintered at 650 °C under vacuum, and HIP posttreated at 650 °C, which exhibited superior optical quality with an in-line transmittance of 87% at 1200 nm. The influences of the vacuum presintering temperature on the phase, densification, microstructure and optical transmission of the ceramics were studied. Since 2021, Wei *et al.* utilized a two-step sintering method comprising air presintering followed by HIP posttreatment to prepare 5 at% Yb:CaF_2 [189], (1, 2, 3, and 5) at% Yb, and 3 at% La:CaF_2 [184] TCs. They investigated the influence of the air presintering temperature on the optical quality and microstructure of ceramics. 3 at% La, 5 at% Yb:CaF_2 TCs presintered at 650 °C and 1 mm in thickness exhibited superior optical quality, with a transmittance of 92.6% at 1200 nm [184]. 5 at% Yb:CaF_2 sample presintered at 650 °C for 2 h and HIP posttreated at 650 °C for 2 h showed the best transparency, with an in-line transmittance of 90% at 1200 nm [189]. Laser testing revealed a QCW laser output, achieving a maximum output power of 0.81 W and a slope efficiency of 22.6% at 1028 nm. In 2023, Guo *et al.* [11] successfully prepared 5 at% Yb:CaF_2 laser ceramics via HP combined with HIP for the first time. The ceramic sample, which was hot-pressed at 575 °C for 2 h and subjected to HIP posttreatment at 600 °C for 3 h, demonstrated superior optical quality, achieving an in-line transmittance of 90.5% at 1200 nm (with a thickness of 3.9 mm). Additionally, the average grain size

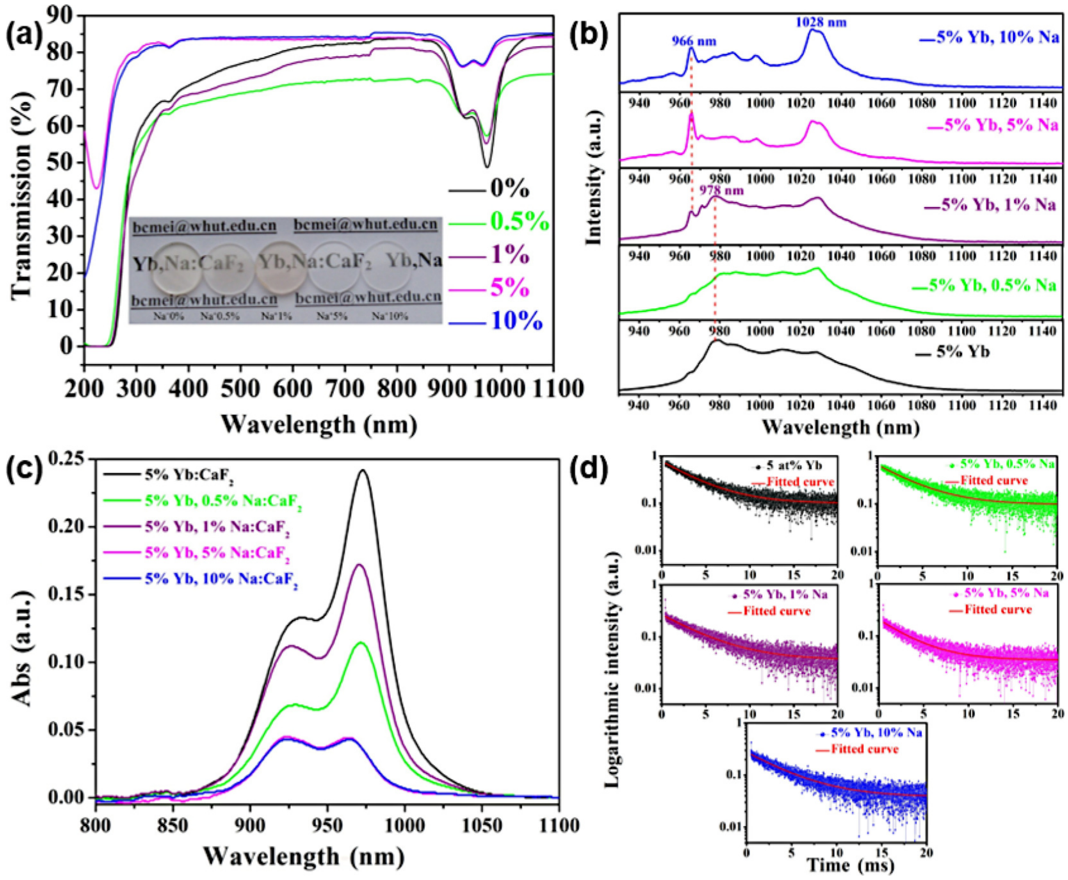

Fig. 11 (a) Photograph and in-line transmittance of 5 at% $Yb:CaF_2$ TCs with different concentrations of NaF, (b) emission spectra of $Yb:CaF_2$ ceramics under 896 nm excitation, and (c) absorption spectra of $Yb:CaF_2$ ceramics. (d) Decay curves of $Yb:CaF_2$ ceramics under 896 nm excitation. Reproduced with permission from Ref. [137], © Elsevier Ltd. 2020.

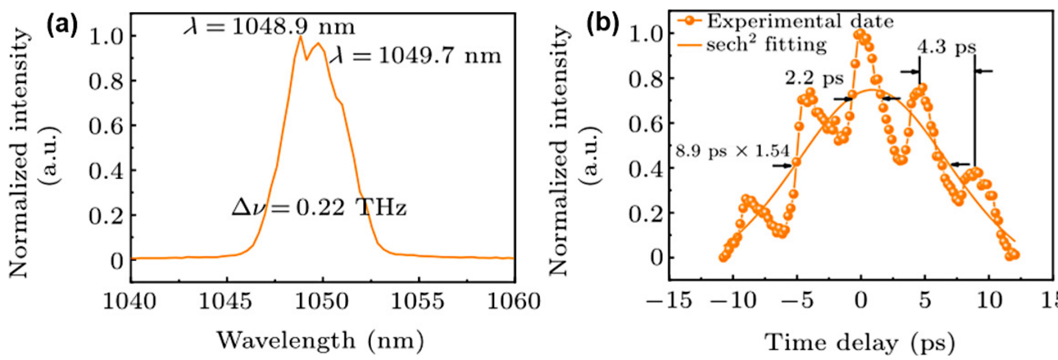

Fig. 12 (a) Measured laser spectrum and (b) the corresponding autocorrelation trace and fitting plot. Reproduced with permission from Ref. [229], © Chinese Physical Society and IOP Publishing Ltd. 2022.

of ceramics was only 470 nm. The maximum output power of ceramics was 1.12 W, with a corresponding slope efficiency of 11.6% (Fig. 13). By 2024, Li *et al.* [192] further investigated the effects of the powder calcination temperature on the microstructure and laser performance of $Yb:CaF_2$ TCs fabricated through air presintering combined with HIP posttreatment. 5 at% $Yb:CaF_2$ TCs, presintered in air at 625 °C from powders calcined in air at 400 °C and subsequently treated with HIP at 600 °C, demonstrated the highest in-line transmittance of 91.5% at 1200 nm (with a thickness of 3.0 mm) and exhibited superior laser performance. Under QCW pumping, the sample achieved a maximum output power of 0.47 W and a peak slope efficiency of 9.2% at 1029 nm.

Research on $Yb:SrF_2$ laser ceramics has also progressed synchronously, but it started relatively late. In 2018, Li *et al.* [134] prepared $Yb:SrF_2$ ceramics by HP method from coprecipitated powders for the first time. The impacts of morphology and particle size on the sintering behavior of $Yb:SrF_2$ nanopowders were examined. Despite achieving a transmittance of 77% at a wavelength of 1200 nm (2 mm in thickness), pores persisted in the ceramics. Furthermore, the spectroscopic and thermal properties of $Yb:SrF_2$ TCs were explored. On this basis, Gao *et al.* [204] applied HP method with coprecipitating powders to fabricate 1–5 at% $Yb:SrF_2$ laser ceramics. 1 at% $Yb:SrF_2$ ceramic sample with a thickness of 2 mm presented the highest transmittance of 85% at 1200 nm. As Yb^{3+} doping concentration increased, both the absorption and emission intensities tended to increase, suggesting the absence of concentration quenching effects in $Yb:SrF_2$ ceramics. However, the decay lifetimes decreased as Yb^{3+} content increased. In 2021, Ling *et al.* [185] prepared 3 at% $Yb:Ca_xSr_{1-x}F_2$

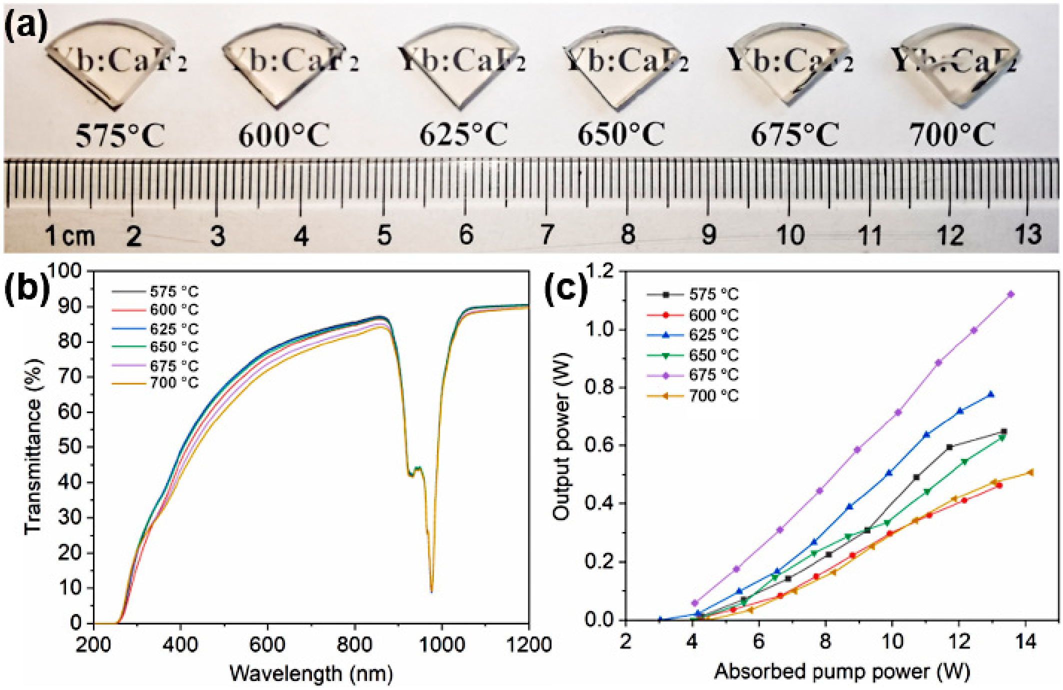

Fig. 13 (a) Photograph, (b) in-line transmittance of 5 at% Yb:CaF_2 TCs hot pressed at different temperatures for 2 h and subjected to HIP at 600 °C for 3 h, (c) QCW laser output power vs. absorbed pump power for ceramic samples. Laser cavity was closed by an output coupler mirror with a transmission of T_{oc} = 12.5%. Reproduced with permission from Ref. [11], © Elsevier B.V. 2023.

(x = 0.1, 0.3, 0.5, 0.7, and 0.9) ceramics via HP from coprecipitated powders. Increasing CaF_2 concentration resulted in a decrease in the lattice constant of 3 at% Yb:$Ca_xSr_{1-x}F_2$. All fabricated 3 at% Yb:$Ca_xSr_{1-x}F_2$ TCs exhibited excellent optical quality, with in-line transmittance exceeding 80% at 1130 nm. With increasing CaF_2 concentration, significant changes in peak shape were observed, accompanied by a gradual increase in the emission bandwidth. The fluorescence lifetimes of all the samples at 1011 nm surpassed 3.25 ms, making them suitable for high-power laser applications.

3.2.2 *Nd^{3+}-doped fluoride laser ceramics*

Using hot forming, Basiev *et al.* [101] prepared Nd:SrF_2 TCs with laser power equivalent to that of single crystals. The maximum output power of ceramics was approximately 16 mW, with a corresponding slope efficiency of 19% under 790 nm pumping. Since 2014, Mei's group from Wuhan University of Technology has been dedicated to investigating Nd^{3+} ion-doped fluoride laser TCs. Lu *et al.* [230] prepared 5 at% Nd:CaF_2 TCs from coprecipitated powders with average particle sizes of approximately 18 nm. The highest transmittance of the sample reached 90% at wavelengths ranging from 250 to 1400 nm for 2 mm thick sample. Owing to their broad absorption bands in the near-infrared (NIR) region, Nd:CaF_2 TCs offer advantages such as reduced dependence on the pump wavelength and temperature control of diode lasers, which holds promise as gain media for the miniaturization of laser devices. On this basis, Sun *et al.* [231] utilized the coprecipitation method to synthesize precursor powders with different Nd-doped concentrations and then fabricated 1–5 at% Nd:CaF_2 ceramics with average grain sizes between 200 nm and 1 μm through HP. 5 at% Nd:CaF_2 ceramic sample presented the highest transmittance of approximately 85% at 1200 nm. The fluorescence quenching effect became more evident with increasing Nd^{3+} ion doping concentration. By 2024, Yi *et al.* [286] further investigated the influence of Nd-doped concentrations on the structural evolution, optical quality, and NIR fluorescence properties of Nd:CaF_2 TCs. The results showed that Nd^{3+} ions positively influence the densification of Nd:CaF_2 transparent ceramics, resulting in improved optical transmittance. Furthermore, an increase in Nd^{3+} concentration correlated with a gradual reduction in the emission lifetime, indicating the occurrence of nonradiative energy transfer among Nd^{3+} ions. Additionally, the concentration quenching mechanism has been confirmed to involve dipole–dipole interactions.

Single Nd^{3+} ions doped in fluoride materials face limitations because of the significant detrimental concentration quenching effect (Fig. 14) [287]. Codoping with buffer ions effectively disrupts clusters, thus mitigating the extent of concentration quenching. Codoping with buffer ions such as Y^{3+}, La^{3+}, or Gd^{3+} readily dissociates [Nd^{3+}–Nd^{3+}] clusters [167,274]. In 2016, Liu *et al.* [167] fabricated 1 at% Nd and 3 at% Y:CaF_2 TCs via HP from coprecipitated powders. For the 2 mm thick ceramic sample sintered at 800 °C, the transmittance at a wavelength of 1200 nm was 85.49%. Additionally, Y^{3+} codoping significantly influences the spectroscopic properties of Nd:CaF_2 ceramics by mitigating the detrimental effects of Nd^{3+} ion clustering. In 2017, Sun *et al.* [169] fabricated Nd,Y:CaF_2 ceramics with different Y^{3+} ion doping concentrations through HP. 1 at% Nd and 2 at% Y:CaF_2 ceramic sample (2 mm in thickness) exhibited the best transparency, with a transmittance of 87% at 1400 nm. Additionally, as the concentration of Y^{3+} ions increased, the emission intensity of Nd,Y:CaF_2 TCs significantly improved, and the concentration quenching effect was suppressed. In 2019, Chen *et al.* [273] prepared 1 at% Nd, 1.8 at% Y:CaF_2, and 1 at% Nd, 2 at% La:CaF_2 ceramics by presintering under a nitrogen atmosphere combined with HIP. The transmittance at 1064 nm for Nd,Y:CaF_2 and Nd,La:CaF_2 ceramics, both with thicknesses of 1 mm, was determined to be 90% and 91%, respectively.

With HP, Xie *et al.* [173] prepared 1 at% Nd and 0–5 at% La:CaF_2 ceramics, with the transmittance of all the ceramics reaching 88% at 1400 nm. Compared with Nd,Y:CaF_2 ceramics, Nd,La:CaF_2 ceramics presented a longer luminescence lifetime, which was attributed to the larger radius of La^{3+} ions at equivalent

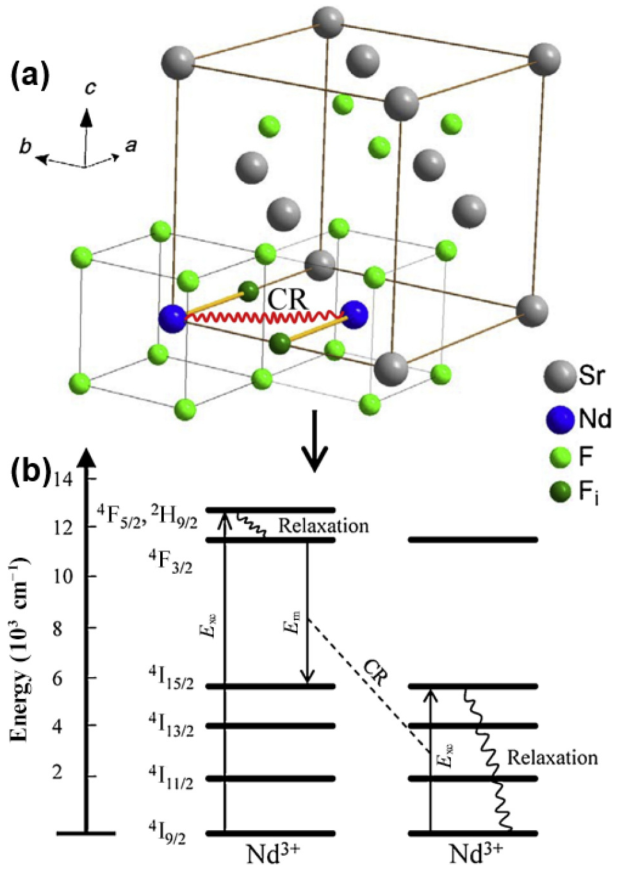

Fig. 14 (a) Schematic of a simple Nd^{3+} cluster in SrF_2 lattice structure and (b) crossrelaxation in energy level diagrams between two Nd^{3+} ions. Reproduced with permission from Ref. [179], © Elsevier Ltd. 2019.

doping concentrations. In 2018, Yi *et al.* [174] further investigated the effects of Nd^{3+} ion doping concentrations on the structural, luminescence, and thermal properties of hot-pressed 0.5–5.0 at% Nd:$(Ca_{0.94}Gd_{0.06})F_{2.06}$ TCs. The emission intensity and transmittance of the sample doped with 1.0 at% Nd^{3+} were the highest. The transmittance of the 2 mm thick sample at 1064 nm was 86%, and the thermal expansion coefficient increased with increasing Nd^{3+} concentration and temperature. After the optimal Nd^{3+} doping concentration was determined to be 1 at%, 1 at% Nd, and 1–10 at% Gd:CaF_2 TCs were further prepared through HP of coprecipitated synthetic nanopowders [175]. All the ceramic samples (2 mm in thickness) exhibited a transmittance of greater than 86% at 1064 nm, and the average grain size decreased slightly with increasing Gd^{3+} concentration. In addition, the incorporation of Gd^{3+} ions significantly enhanced the luminescence characteristics of Nd:CaF_2 TCs by effectively suppressing [Nd^{3+}–Nd^{3+}] clusters. Furthermore, the segregation tendency of rare earth elements at grain boundaries escalates with increasing rare earth ion concentration, indicating an inevitable increase in scattering at grain boundaries due to element segregation in highly doped samples [191]. Consequently, this phenomenon elucidated the diminished transmittance observed in 1 at% Nd and 10 at% Gd:CaF_2 compared with the other samples.

Compared with those of Y^{3+}, La^{3+}, and Gd^{3+} codoping, the tuning mechanisms of Sr^{3+} codoping ions are different. In the case of Sr^{2+} codoping, luminescence enhancement occurs as a result of the disruption in the symmetry of the local field surrounding Nd^{3+}, thereby favoring the 4f → 4f transitions (Fig. 15). Conversely, in Y^{3+} codoping, the primary mechanism involves the generation of more active [Nd^{3+}–Y^{3+}] centers, effectively mitigating concentration quenching. In 2016, Zhu *et al.* [196] further successfully prepared $Ca_{0.85}Sr_{0.1}Nd_{0.05}F_{2.05}$ ceramics with a mean grain size of 0.5 μm through HP. The in-line transmittance of the ceramic sample (2 mm in thickness) reached 86% at wavelengths ranging from 250 to 1400 nm. In addition, the emission intensity of $Ca_{0.85}Sr_{0.1}Nd_{0.05}F_{2.05}$ sample was significantly greater than that of Nd:CaF_2 sample, which was attributed to the modulation effect of Sr^{2+} ions. With the aid of HP, Zhou *et al.* [180] successfully prepared Nd:$Ca_{1-x}Sr_xF_2$ (x = 0, 0.1, 0.2, 0.25, 0.3, and 0.5) TCs via coprecipitation of synthetic nanopowders. As x increased from 0 to 0.2 in Nd:$Ca_{1-x}Sr_xF_2$ ceramics, there was a notable increase in the luminescence intensity, emission lifetime, and emission cross section. However, this variation scarcely impacted concentration quenching. The luminescence intensities and emission lifetimes between samples with x values of 0.2 and 0.25 exhibited minimal disparity, suggesting the probable formation of SrF_2 phase in the $x = 0.25$ sample.

By ceramizing single crystals, Jiang *et al.* [107] successfully prepared Nd:$Ca_{1-x}Y_xF_{2+x}$ laser ceramics with the same optical properties as those of precursor single crystals. CW laser operation, yielding an output power of 35 mW, was successfully achieved via a fiber-coupled laser diode emitting at a central wavelength of approximately 808 nm (Fig. 16). They subsequently

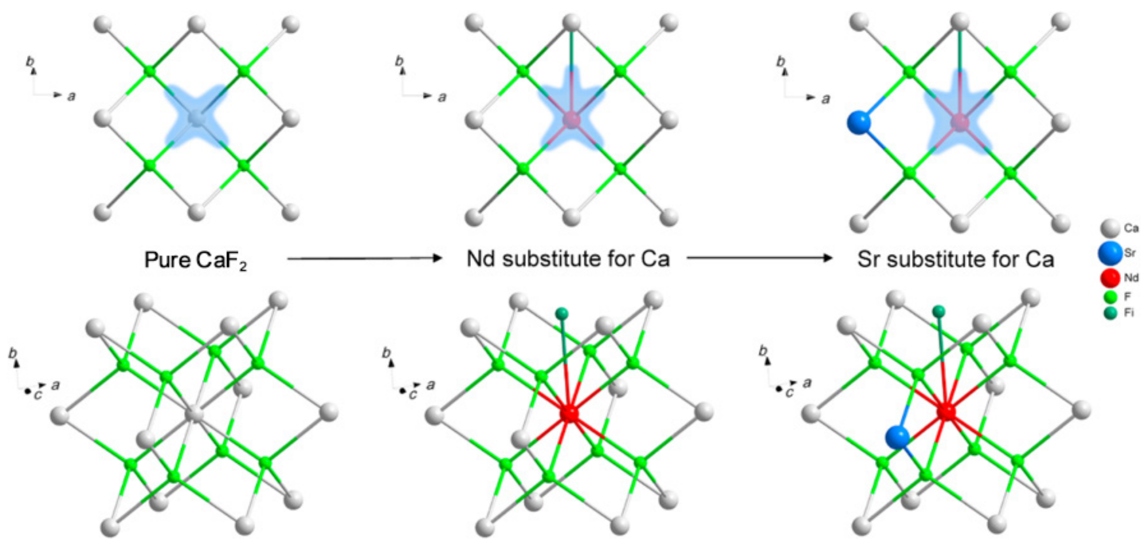

Fig. 15 Schematic of symmetry breaking mechanism for Sr^{2+} codoping. Reproduced with permission from Ref. [180], © Elsevier B.V. 2019.

清華大学出版社 Tsinghua University Press | SciOpen

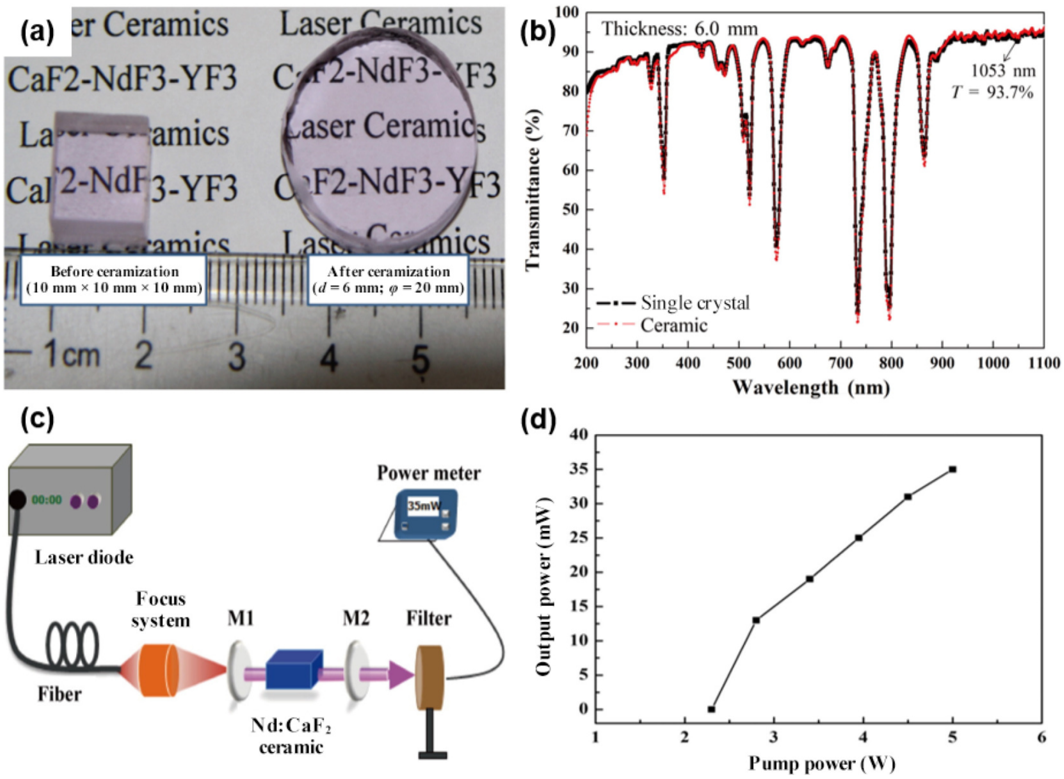

Fig. 16 (a) Photograph, (b) in-line transmittance of Nd:$Ca_{1-x}Y_xF_{2+x}$ single crystals before and after the ceramization process, (c) schematic of Nd:$Ca_{1-x}Y_xF_{2+x}$ ceramic laser, and (d) output power of Nd:$Ca_{1-x}Y_xF_{2+x}$ ceramic laser lasing at 1053 nm as a function of absorbed pump power when an output coupler with a transmission of 3% is used. Reproduced with permission from Ref. [107], © Elsevier Ltd. 2016.

investigated the effects of the deformation rate on the crystallization behavior, microstructures, mechanical properties, and optical performance of 0.8 at% Nd and 5 at% Y:CaF_2 ceramics [266]. Nd,Y-codoped CaF_2 ceramic sample (Δa = 62%) demonstrated exceptional characteristics, including high transparency (transmittance above 91% over a thickness of 3 mm, ranging from 250 to 1200 nm), minimal light scattering, superior fracture toughness (with K_{IC} of approximately 0.71 MPa·m$^{1/2}$), intense fluorescence emission, prolonged lifetime (τ = 348.72 μs), and a wide full width at half maximum (FWHM) of 29.2 nm. These attributes make it a promising candidate for high-power laser applications.

High-entropy fluoride ceramics have evolved from the concept of high-entropy alloys (HEAs), which are characterized as solid solutions featuring a single-crystal structure comprising five or more metallic elements [288]. Each element is incorporated in an isoatomic or near-isoatomic ratio, typically ranging from 5 to 35 at% [289,290]. Nd^{3+} and various lanthanide cations, such as La^{3+}, Y^{3+}, Gd^{3+}, and Lu^{3+}, can be effectively doped into fluoride transparent ceramics, as mentioned above [167,169,173–175,266]. Fluoride has a typical fluorite-type cubic structure with numerous interstitial sites, providing a broad transmission range along with a low phonon energy and refractive index. Consequently, rare-earth-doped fluoride serves as an ideal substrate system for high-entropy TCs [11,189]. In 2020, Chen and Wu [291] successfully fabricated the first high-entropy transparent fluoride laser ceramics with a $CeNdCaSrBaF_{12}$ (CNCSBF) composition. The ceramic sample with an average grain size of 20 μm exhibited the highest transmittance of approximately 60% at 1000 nm. A NIR photoluminescence (PL) emission band was detected at 1057 nm, accompanied by a visible-range PL emission band at 440 nm (Fig. 17). These findings suggest that distinctive optical properties are suitable for laser-based applications. Chen *et al.* [15] subsequently prepared Nd_x:$(La_{0.05}Lu_{0.05}Gd_{0.05}Y_{0.05})Ca_{0.8-x}F_{2.2+x}$ (x = 0.0–1.2) high-entropy TCs through HP coprecipitation of synthetic powders. The $Nd_{0.5}$:$(La_{0.05}Lu_{0.05}Gd_{0.05}Y_{0.05})Ca_{0.3}F_{2.7}$ ceramic sample exhibited the best transmittance of 86% at 1200 nm. The average grain sizes of fabricated high-entropy TCs initially decreased and then increased with increasing Nd^{3+} doping concentration. Additionally, the luminescence intensity and fluorescence lifetime of 1.0 at% Nd:$(La_{0.05}Lu_{0.05}Gd_{0.05}Y_{0.05})Ca_{0.8}F_{2.2}$ TCs surpassed those of 1.0 at% Nd:CaF_2.

In addition to the research on Nd:CaF_2 laser ceramics, investigations of Nd:SrF_2 TCs are also being conducted simultaneously. In 2015, Li *et al.* [274] prepared 0.15 at% Nd and 5 at% Y:SrF_2 ceramics by deforming Nd,Y:SrF_2 single crystals. The ceramic sample achieved a peak output power of 0.583 W when subjected to an absorption pump power of 2.164 W, corresponding to a slope efficiency of 31.9%. Additionally, the mechanical properties of Nd,Y:SrF_2 ceramics surpassed those of single crystals. On the basis of these findings, Zhang *et al.* [275] further investigated the laser performance of 0.15 at% Nd and 5 at% Y:SrF_2 ceramics in both CW and Q-switched regimes. During CW operation, a dual-wavelength laser peaking at 1050.5 and 1058.0 nm was achieved, delivering a maximum average output power of 750 mW. In passively Q-switched operation, the shortest pulse width obtained was 169 ns, with a corresponding single pulse energy and peak power of 19.2 μJ and 113 W, respectively. Therefore, Nd:Y:SrF_2 laser ceramics exhibited promising performance in the 1.06 μm region, making them suitable for high-power ultrashort pulse generation. Furthermore, Qin *et al.* [201] compared 0.5 at% Nd and 5 at% Y:SrF_2 TCs fabricated through two methods—hot-forming and HP techniques—to single crystals. Compared with hot-formed ceramics and single crystals, hot-pressed ceramics have superior mechanical properties but exhibit low density, reduced

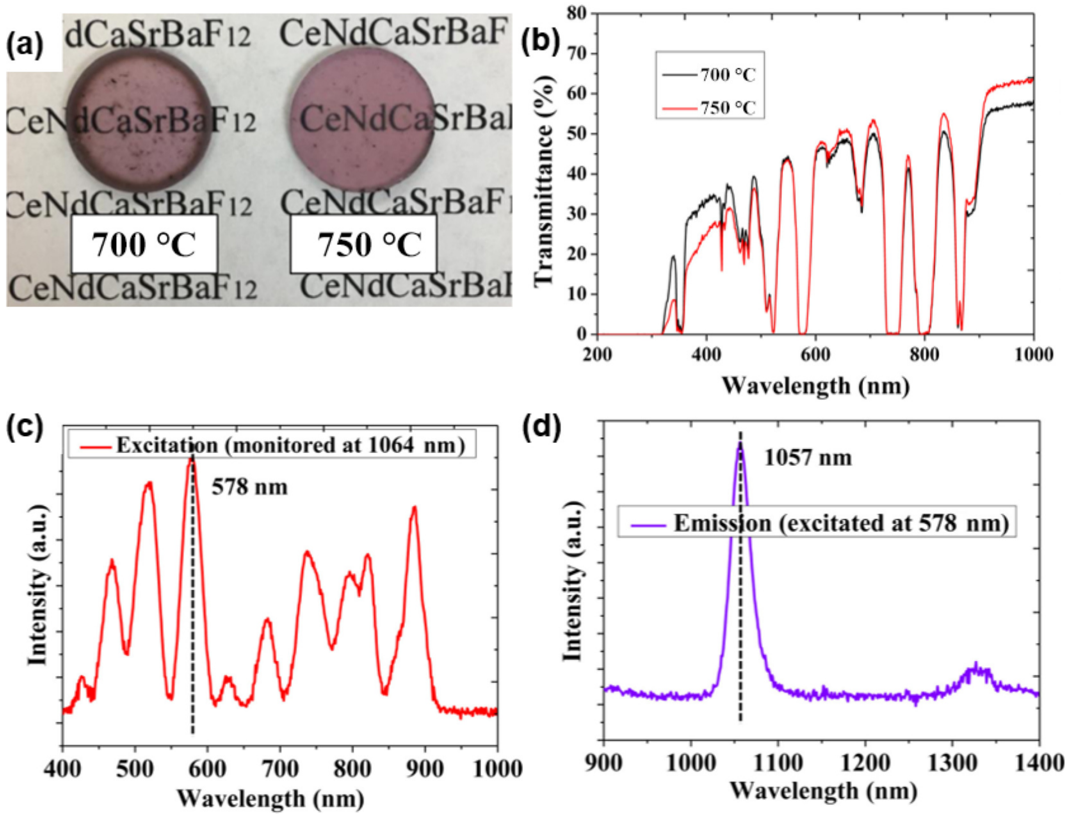

Fig. 17 (a) Photograph, (b) in-line transmittance of CNCSBF TCs sintered at 700 and 750 °C by HP, (c) excitation spectrum monitored at 1064 nm, and (d) emission spectrum excited by 578 nm radiation. Reproduced with permission from Ref. [291], © The American Ceramic Society 2019.

transmittance, and failure to achieve laser output. The hot-formed ceramics displayed enhanced mechanical properties and laser performance relative to those of the single crystals. In 2019, Jiang *et al.* [110] applied the single-crystal ceramization (SCC) technique combined with thermal drive-induced grain regrowth (TDIGR) treatment to fabricate Nd,Gd:SrF_2 ceramics. The results indicated that TDIGR could effectively address the reclustering of Nd^{3+} ions during SCC without affecting the transmittance of ceramics.

Zhou *et al.* [200] utilized the coprecipitation method to synthesize Nd:SrF_2 and SrF_2 nanopowders. The effects of the reactant concentration and Nd^{3+} doping concentration on the morphology and size of the powders were investigated. The hot-pressed ceramic sample (2 mm thick) exhibited a transmittance of 80% at 1060 nm. Furthermore, Zhou *et al.* [215] fabricated 0.5–5 at% Nd:SrF_2 ceramics through HP. 5 at% Nd:SrF_2 ceramic sample (2.5 mm in thickness) exhibited the highest transmittance of 85.3% at 1060 nm. The emission spectra indicated concentration quenching at Nd^{3+} concentrations of 1%–2%. The optimal Nd^{3+} doping level for achieving the desired spectral properties in Nd:SrF_2 transparent ceramics appeared to be approximately 1%. By applying Judd–Ofelt theory, Zhou *et al.* [179] analyzed the optical performance of Nd^{3+} in SrF_2 and CaF_2 hosts. Nd:SrF_2 ceramics exhibited a reduced line strength, extended radiative lifetime, and decreased Ω_2 value, indicative of increased ionic Nd^{3+}-ligand bonding and enhanced symmetry in Nd^{3+} environment. These characteristics facilitate population inversion and robust emission, thereby enhancing laser performance. In addition, Zhu *et al.* [203] investigated the effect of La^{3+} ion codoping concentration on the microstructure and spectral properties of 1 at% Nd:SrF_2 laser ceramics fabricated via HP. The addition of La^{3+} as a buffer ion clearly enhanced the absorption and emission intensity by suppressing [Nd^{3+}–Nd^{3+}] clusters. In 2021, Liu *et al.* [210] first fabricated a novel transparent SrF_2/Nd:SrF_2/SrF_2 composite ceramic sample with a sandwich-like laminar configuration via HP. The transmittance of 2 mm thick SrF_2/Nd:SrF_2/SrF_2 composite sample at 500 and 1200 nm was approximately 49.6% and 62.3%, respectively. Additionally, the thermal conductivities of the ceramic samples were greater than those of Nd:SrF_2 sample. In 2022, Zhou *et al.* [216] proposed a novel coprecipitation method, spray coprecipitation, to fabricate Nd:SrF_2 TCs with high optical quality. Compared with the traditional coprecipitation method, the nanoparticles synthesized via the spray coprecipitation method displayed a more uniform and diminutive morphology, and Nd:SrF_2 ceramic sample produced through HP using these nanoparticles demonstrated superior transmittance across all wavelengths.

In addition to codoping with buffer ions such as Y^{3+}, Gd^{3+}, and La^{3+} to disperse Nd^{3+} ion clusters within the matrix materials and mitigate concentration quenching, another approach involves introducing other rare earth ions (such as Yb^{3+}, Ce^{3+}, or Cr^{3+}) as sensitizers to increase the luminescence efficiency of Nd^{3+} [292–294]. In 2023, Zhang *et al.* [14] fabricated 0.5–2.0 at% Nd and 0.6 at% Ce:SrF_2 ceramics with high optical quality. 2.0 at% Nd and 0.6 at% Ce:SrF_2 ceramic sample (2 mm in thickness) exhibited the highest transmittance of 82% at 400 nm and 92.5% at 1054 nm. The incorporation of cerium ions altered the crystal field environment surrounding Nd^{3+} ions, leading to a redshift in the emission peak from $^4F_{3/2}$ → $^4I_{11/2}$. This adjustment effectively mitigated the phenomenon of concentration quenching. The simplified energy levels and possible energy transfer model of the Nd,Ce:SrF_2 system are shown in Fig. 18.

Few studies on BaF_2-based laser ceramics have been reported. In 2018, Li *et al.* [143] successfully fabricated 5 at% Nd:BaF_2 TCs

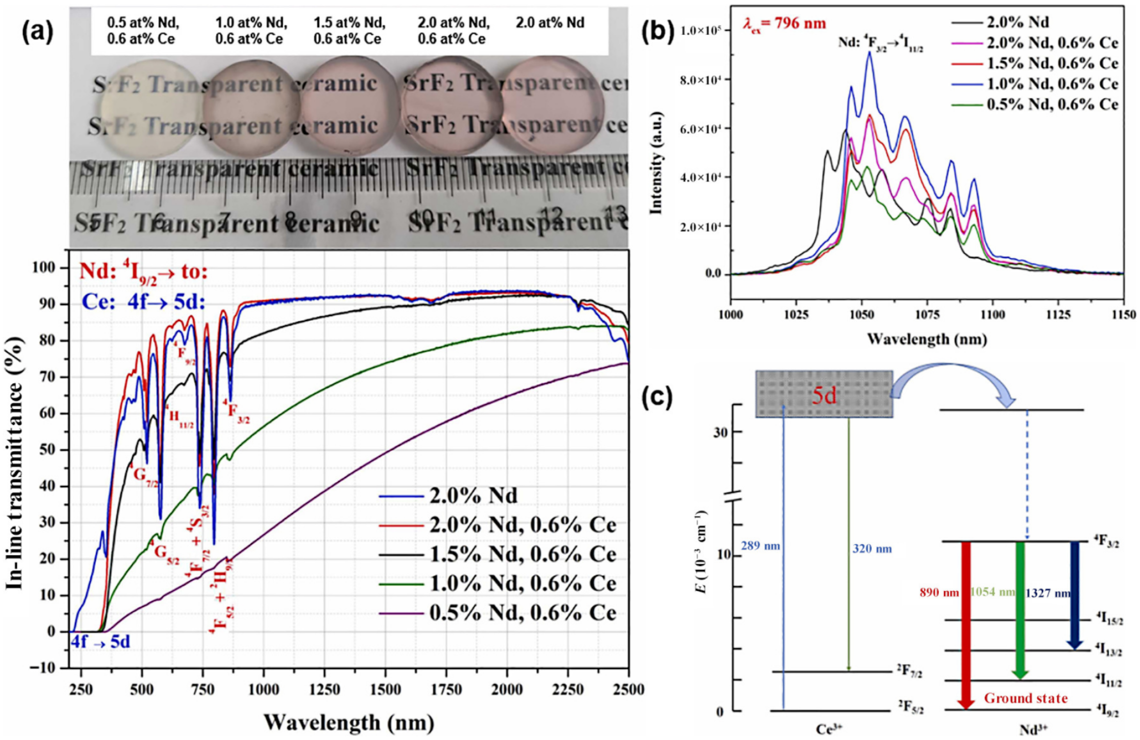

Fig. 18 (a) Photograph and transmittance of Nd,Ce:SrF_2 ceramics, (b) emission spectra of Nd,Ce:SrF_2 ceramics under 796 nm excitation at room temperature, and (c) simplified energy levels and possible energy transfer model of Nd,Ce:SrF_2 system. Reproduced with permission from Ref. [14], © Elsevier Ltd. 2023.

via a one-step vacuum sintering method at a temperature of 1200 °C for 10 h. Nd:BaF_2 powders with particle sizes ranging from 100 to 200 nm were synthesized through the coprecipitation method, followed by washing by pumping filtration and low-temperature calcination in argon. The resulting ceramic sample, with a thickness of 1 mm and a large average grain size of 420 μm, achieved a maximum transmittance of approximately 70% within the infrared wavelength range. Additionally, it exhibited an emission peak located at 1058 nm, which was excited by 808 nm light.

3.3 2–3 μm band rare earth ion-doped fluoride laser ceramics

Er^{3+} and Ho^{3+} ions possess multiple energy levels, resulting in emission peaks spanning a broad wavelength range from the visible to the infrared spectra. Erbium-doped and holmium-doped lasers are crucial in various fields, including eye-safe research, optical communications, medical treatments, and laser detection [5]. Research on other 2–3 μm band rare earth ion-doped fluoride laser ceramics is limited to materials such as Tm:CaF_2 [119–121], and a detailed description is not provided here.

3.3.1 *Er^{3+}-doped fluoride laser ceramics*

Using a hot-forming technique, Šulc *et al.* [122] prepared Er:CaF_2 ceramics with a 3% slope efficiency of MIR (2.7 μm) radiation under pulsed 968 nm laser diode pumping in 2013. By SCC, Jiang *et al.* [123] successfully prepared 3 at% Er:CaF_2 TCs with excellent optical quality. The samples displayed a distinct polycrystalline structure alongside impeccable transmittance and exceptional MIR performance, surpassing those of hot-pressed and hot-formed ceramics.

In 2011, Zhi *et al.* [157] synthesized Er:CaF_2 nanopowders with different doping concentrations via the coprecipitation method. An increasing Er^{3+} doping concentration resulted in a reduced grain size and crystallinity but concurrently led to a significant increase in the lattice constant due to the formation of interstitial fluorine ions. The fluorescence intensity of Er:CaF_2 nanoparticles initially increased but then decreased with increasing dopant concentration, indicating concentration quenching. Using HP, Zhou *et al.* [163] fabricated 5 at% Er:CaF_2 TCs with an average grain size of 8 μm and added LiF as a sintering additive. The transmittance of the ceramic sample was nearly 85% at visible and NIR wavelengths. By hot-pressing coprecipitating synthetic precursor powders, Liu *et al.* [232] prepared 1 and 5 at% Er:CaF_2 TCs with a mean grain size of less than 1 μm in 2014. Er:CaF_2 ceramic sample reached a transmittance of 87% at 1200 nm. On the basis of Judd–Ofelt theory, Xing *et al.* [233] computed radiative transition probabilities, radiative lifetimes, and integrated emission cross-sections of several Er^{3+} transitions in CaF_2 TCs fabricated via HP and measured the absorption spectra, emission spectra, and decay times.

On the above basis, Liu *et al.* [164] further investigated the influence of Er^{3+} doping concentrations on the microstructure and spectral properties of Er:CaF_2 TCs fabricated with HP. 5 at% Er:CaF_2 ceramic sample (2 mm in thickness) presented the best transmittance, 85% at 900 nm, and a low Er^{3+} ion doping concentration (< 5 mol%) effectively reduced the grain size. On the basis of the above research progress, Liu *et al.* [176] further studied the influence of Er^{3+} doping concentration on the microstructure and MIR properties of Er:CaF_2 ceramics prepared via HP. The results demonstrated that the emission intensities of NIR and MIR luminescence were significantly increased. The intensified emission at 2.7 μm and the shortened NIR fluorescence lifetimes suggested that a high concentration of Er^{3+} ions was advantageous for mitigating the self-termination effect and achieving a 2.7 μm laser output. In 2019, 1–5 mol% Er:CaF_2 ceramics with excellent optical quality were prepared by Yang *et al.* [177] via hot-pressing precursor powders synthesized via the coprecipitation method. For the 2 mm thick samples, 2 mol%

Er:CaF_2 sample presented the best transmittance, reaching 75% at 400 nm and 93% at 2000 nm, which was very close to the theoretical transmittance (approximately 94%). In addition, strategies for different wavelengths of excitation were discussed. Compared with single-wavelength excitation, two-wavelength excitation clearly increased the intensity of upconversion (UC) emission. This enhancement arises from reduced energy losses due to photon-energy level transition mismatch and multiwavelength relaxation, facilitated by the synergistic effect of 980 and 808 nm photons (Fig. 19).

Using the two-step sintering method of air presintering combined with HIP posttreatment, Guo *et al.* successfully fabricated fine-grained 1 at% Er:CaF_2 [128] and 1 at% Er:SrF_2 [142] laser TCs with excellent optical quality. 1 at% Er:CaF_2 TCs, presintered at 625 °C and subsequently HIP-treated at 650 °C, demonstrated the highest optical quality, with an in-line transmittance of 90.5% at a wavelength of 1600 nm (Fig. 20). This finding suggested that a presintering temperature of 625 °C, coupled with a HIP posttreatment temperature of 650 °C, represented the optimal processing conditions for achieving superior transparency in 1 at% Er:CaF_2 ceramics.

In addition to pure phase ceramics, composite ceramics are also increasingly favored by researchers. By combining multistep dry pressing and HP sintering methodologies, Liu *et al.* [236] successfully prepared Er(2%):CaF_2/Er(5%):CaF_2/Er(2%):CaF_2 composite ceramics with a 150–200 μm thick transition interface. 1.5 mm thick ceramic sample exhibited an optical transmittance of 44.9% at 500 nm and 53.6% at 1200 nm and had much higher thermal conductivities than Er:CaF_2 ceramics.

By HP chemically derived powders at 700 °C for 40 h, 5 at% Er:SrF_2 TCs with high optical quality were successfully fabricated by Liu *et al.* [198] in 2018. The grain growth kinetics of Er:SrF_2 were elucidated. This was the first confirmation of lattice diffusion as the grain growth mechanism in Er:SrF_2 TCs, and Er:SrF_2 TCs achieved a peak in-line transmittance of 92% at 2000 nm. By hot-pressing ball-milling mix powders, 0–10 wt% Er:SrF_2 TCs with high optical transparency were fabricated by Liu *et al.* [208]. The incorporation of ErF_3 effectively reduced the average grain size and positively influenced the increase in the Vickers hardness of Er:SrF_2 TCs. 5 wt% Er:SrF_2 ceramic sample exhibited the best transmittance of 87.9% and 89.5% at 500 and 1200 nm, respectively. In 2021, Yang *et al.* [186] studied the effects of

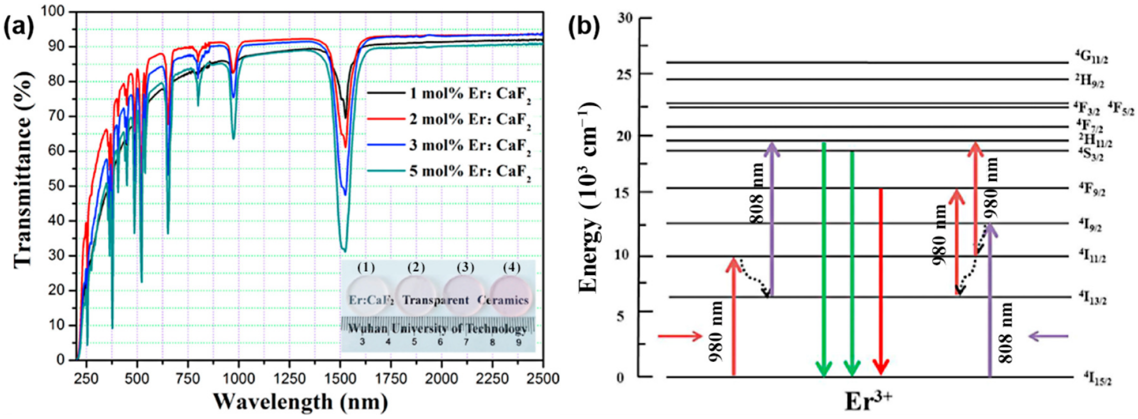

Fig. 19 (a) Transmittance and photograph of Er:CaF_2 ceramics (2 mm in thickness), (b) energy level diagram of UC mechanism in Er:CaF_2 upon two-wavelength (980 nm + 808 nm) excitation. Reproduced with permission from Ref. [177], © Elsevier B.V. 2019.

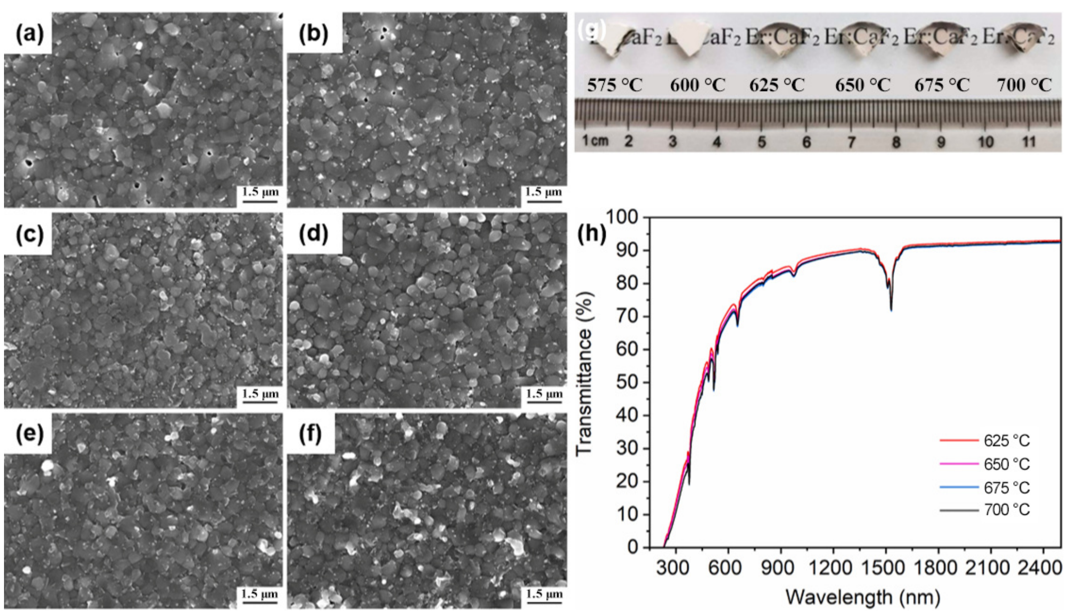

Fig. 20 FESEM micrographs of 1 at% Er:CaF_2 ceramics presintered in air at different temperatures: (a) 575, (b) 600, (c) 625, (d) 650, (e) 675, and (f) 700 °C. (g) Photograph and (h) intraline transmittance of 1 at% Er:CaF_2 ceramics (2.8 mm thick) air presintered at different temperatures and subjected to HIP at 650 °C. Reproduced with permission from Ref. [128], © Elsevier B.V. 2022.

https://doi.org/10.26599/JAC.2024.9220986

different sintering temperatures and doping concentrations on Er:SrF_2 TCs. The best transparency was achieved by 1 at% Er:SrF_2 sample (2 mm in thickness) sintered at 900 °C, with values of 67% and 92% at 400 and 2400 nm, respectively. Compared with Er:CaF_2, the green emission of Er:SrF_2 ceramics was much stronger, whereas the red emission of Er:SrF_2 ceramics was almost the same as that of Er:CaF_2 ceramics. The upconversion luminescence lifetime of the Er:SrF_2 ceramics was longer than that of Er:CaF_2. Liu *et al.* [212] further investigated the effects of the sintering temperature and soaking time on the microstructure evolution of 5 wt% Er:SrF_2 fabricated via HP. Er:SrF_2 ceramic sample (2 mm thick) hot-pressed at 900 °C for 2 h demonstrated the highest transmittance, with values of 90.4% at 500 nm and 91.7% at 1200 nm. The grain growth kinetic mechanism observed in the ceramics during the final sintering stage was associated with solute drag.

In 2023, a series of 1 at% Er:SrF_2 ceramics were successfully fabricated through air presintering at 550–650 °C for 2 h, followed by HIP posttreatment at 600 °C for 2 h under 100 MPa Ar [142]. The results demonstrated that a higher presintering temperature range of 550–650 °C facilitated the generation of pure phase ceramics and the substitution of Er^{3+} for Sr^{2+} in the lattice structure. The in-line transmittance of 1 at% Er:SrF_2 ceramics (2.5 mm in thickness) presintered at 650 °C and subsequently subjected to HIP posttreatment reached 83.4% at 2500 nm. The luminescence lifetime of 1 at% Er:SrF_2 ceramics at 1530 nm was 49.6 ms.

Guo *et al.* [147] first utilized a novel and environmentally friendly method (CSP) for the preparation of Er:SrF_2 TCs at ultralow temperatures. 5 at% Er:SrF_2 nanoparticles were synthesized through the coprecipitation method. Er:SrF_2 TCs prepared at 300 °C and 468 MPa exhibited the best transmittance in the visible range of 48.59%, whereas the transmittance at 1100 nm reached 76.94% (Fig. 21). A reduction in the sintering temperature of SrF_2 TCs by CSP of at least 500 °C was achieved compared with that of the conventional preparation process.

As mentioned above [173,202,266,274], strong cross-relaxation phenomena were also observed between Er^{3+} ions, and it is imperative to mitigate extensive clustering and enhance the spatial separation of active ions within fluoride matrix materials. In 2013, Li *et al.* [160] fabricated 5 at% Er, 0–1.5 at% Na:CaF_2 TCs through hot-pressing coprecipitating powders. The results demonstrated that the introduction of Na ions into Er:CaF_2 TCs facilitated the formation of a charge-neutralized [Er^{3+}–Na^{+}] structure, thereby impeding [Er^{3+}–Er^{3+}] clustering. Consequently, the enhanced emission intensity and fluorescence lifetime could be ascribed to the codoping of Na ions, which mitigated the cluster formation of Er^{3+} and reduced the fluorescence quenching effect. On this basis, Liu *et al.* [162,235,267] further investigated the effect of Yb^{3+} ions on the spectral properties of Er:CaF_2 TCs fabricated via HP. The best transparency was achieved by 1 at% Er, 5 at% Yb:CaF_2 ceramics (2 mm in thickness), with 90% transparency in NIR spectral region. The grain size decreased with increasing Yb concentration, whereas the increase in the green, red, and NIR emission intensities with increasing Yb concentration was attributed to modifications in the interionic distance and increased energy transfer between Yb and Er ions [267]. Li *et al.* [214,234,237] subsequently investigated the effects of Y^{3+}, Dy^{3+}, and Ho^{3+} codoping on Er:CaF_2 and Er:SrF_2 ceramics prepared via HP.

3.3.2 Ho^{3+}-doped fluoride laser ceramics

Popov *et al.* [265] successfully prepared $Ca_{1-x}Ho_xF_{2+x}$ (x = 0.001–0.03) ceramics by hot forming single crystals in 2012. The results showed that doping with rare earth fluorides, accompanied by the formation of solid solutions, sharply decreased the thermal conductivity of CaF_2. In 2017, Li *et al.* [238] used HP to prepare 2 at% Ho:CaF_2 TCs with precursor powders synthesized via the chemical coprecipitation method. The transmittance within NIR range closely paralleled that of pure CaF_2 single crystals. The principal emission band of Ho^{3+} ions in CaF_2 was centered at 2030 nm, indicating that the prepared Ho:CaF_2 ceramics hold promise as laser materials for 2.0 μm solid-state laser applications. Subsequently, they fabricated $Ca_{1-x}Ho_xF_{2+x}$ (x = 0.5, 1.0, 2.0, 3.0, and 5.0 mol%) ceramics through HP method [239]. 2 mol% Ho:CaF_2 ceramics showed the best transmittance at 1200 nm, reaching a maximum value of 85% (2 mm thickness). The emission intensity at 2 μm initially increased but then decreased

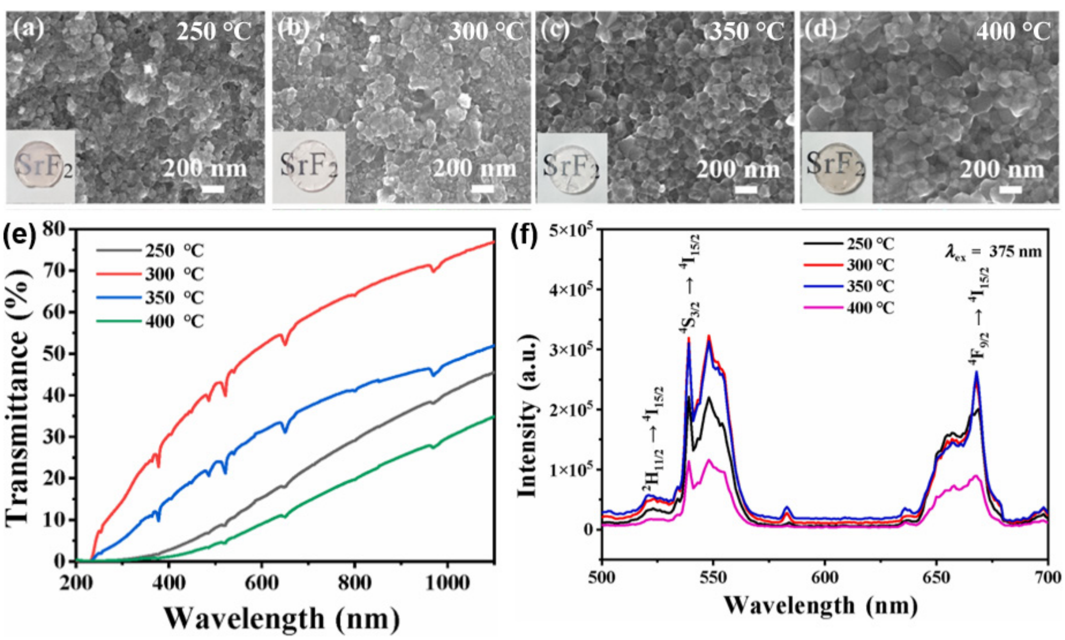

Fig. 21 SEM profiles of preparation of 5 at% Er:SrF_2 TCs at different sintering temperatures: (a) 250 °C, (b) 300 °C, (c) 350 °C, and (d) 400 °C. (e) Transmittance and (f) emission spectra of 5 at% Er:SrF_2 TCs. Reproduced with permission from Ref. [147], © Elsevier B.V. 2023.

with increasing concentrations of Ho^{3+} ions. The fluorescence lifetime at 2030 nm was also examined, further indicating the potential of Ho:CaF_2 TCs as candidates for 2.0 μm laser emission materials.

Additionally, via the HP method, Yang *et al.* [214] prepared 3 at% Er^{3+}, *x* at% Ho^{3+}:SrF_2 (x = 0, 0.05, 0.1, 0.5, 1, and 2) TCs with precursor powders synthesized via the coprecipitation method in 2022. The best transmittance was 93% at a wavelength of 2500 nm for 3 at% Er^{3+} and 2 at% Ho^{3+}:SrF_2 sample with a thickness of 2 mm, which almost reached the theoretical transmittance of SrF_2 TCs (93.7%). The transmittance decreased sharply in the visible range because of Rayleigh scattering. Furthermore, following the introduction of Ho^{3+}, both MIR and NIR emissions of Er^{3+} were suppressed. Nevertheless, the disparity in lifetimes between $^4I_{11/2}$ and $^4I_{13/2}$ levels of Er^{3+} emissions at 2.7 μm notably diminished from 8.50 to 1.12 ms as Ho^{3+} concentration increased from 0.05 to 2 at%, underscoring the significant depopulation efficacy of Ho^{3+}. This depopulation effect of Ho^{3+} stemmed from two energy transfer processes: ET1 involving $^4I_{11/2}$ (Er^{3+}) → $^5I_6$ (Ho^{3+}) and ET2 involving $^4I_{13/2}$ (Er^{3+}) → $^5I_7$ (Ho^{3+}) (Fig. 22). These results demonstrated that incorporating Ho^{3+} ions at an appropriate doping concentration enhanced the potential for achieving 2.7 μm laser output in Er^{3+}:SrF_2 TCs.

4 Conclusions and outlook

This review provides an overview of the research progress, precursor powder synthesis, and ceramic fabrication of fluoride laser ceramics. Among existing laser materials, fluoride ceramics demonstrate promising comprehensive performance, including low phonon energy, long fluorescence lifetime, wide emission band, good thermal–optical properties, and excellent size scalability. Notably, ceramic synthesis technology enables the fabrication of high-concentration and uniformly doped rare earths compared with single crystals. Table 4 summarizes the laser outputs of currently reported fluoride ceramics, showing successful lasing in both the visible and infrared spectral regions. However, fluoride ceramics exhibit relatively lower output power

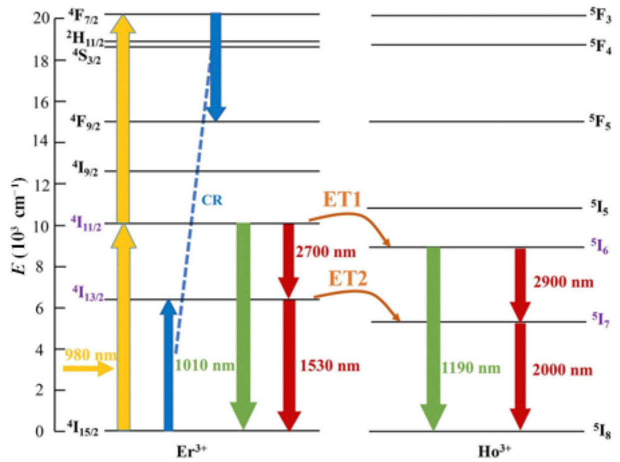

Fig. 22 Energy level diagram of Er^{3+} and Ho^{3+} with the possible energy transfer processes. Reproduced with permission from Ref. [214], © Elsevier Ltd. 2021.

Table 4 Summary of fluoride ceramic laser outputs

Ceramic	Compaction method	Laser output	Ref.
CaF_2–SrF_2–YbF_3	Hot forming	η_{sl} = 45%, P = 1.7 W, CW	[105]
3 at%Yb:CaF_2	Hot forming	η_{sl} = 30%, P = 0.7 W, CW	[116]
5 at%Yb:CaF_2	Hot forming	η_{sl} = 35%, P = 1.2 W, CW	[116]
3 at%Yb:CaF_2–LaF_3	Hot forming	η_{sl} = 35%, P = 1.09 W, CW	[280]
4 at%Yb:CaF_2	Air sintering	η_{sl} = 43%, P = 1.6 W, CW	[281]
Yb:CaF_2–LaF_3	Air sintering + HIP	η_{sl} = 73.1%, P = 3.97 W, CW	[283]
Yb:CaF_2–LaF_3	Air sintering + HIP	η_{sl} = 69.5%, P = 4.36 W, CW	[67]
5 at%Yb:CaF_2	Vacuum sintering + HIP	η_{sl} = 23.6%, P = 0.9 W, QCW	[127]
5 at%Yb:CaF_2	HP	η_{sl} = 26%, P = 0.809 W, CW	[181]
3 at%Yb, 1 at%Y:CaF_2	HP	η_{sl} = 29.3%, P = 1.1.6 W, CW	[182]
3 at%Yb, 1 at%Y:CaF_2	HP	η_{sl} = 5.1%, P = 0.31 W, CWML	[229]
5 at%Yb:CaF_2	Air sintering + HIP	η_{sl} = 22.6%, P = 0.81 W, QCW	[189]
5 at%Yb:CaF_2	Air sintering + HIP	η_{sl} = 9.2%, P = 0.47 W, QCW	[192]
5 at%Yb:CaF_2	HP + HIP	η_{sl} = 11.6%, P = 1.12 W, QCW	[11]
1 at%Nd, 2 at% La:CaF_2	Nitrogen sintering + HIP	η_{sl} = 1.9%, P = 2.6 W, CW	[273]
0.6 at%Nd, 10 at%Y:CaF_2	Hot forming	η_{sl} = 1.0%, P = 35 mW, CW	[107]
0.5 at%Nd:SrF_2	Hot forming	η_{sl} = 19%, P ≈ 16 mW, CW	[101]
0.15 at%Nd, 5 at%Y:SrF_2	Hot forming	η_{sl} = 31.9%, P = 0.583 W, CW	[274]
0.15 at%Nd, 5 at%Y:SrF_2	Hot forming	η_{sl} = 31.5%, P = 0.75 W, CW	[275]
1 at%Nd, 1.8 at%Y:CaF_2	Nitrogen sintering + HIP	η_{sl} = 1.0%, P = 3.7 W, CW	[273]
Pr:SrF_2	Hot forming	η_{sl} = 9%, P = 7.5 mW, CW	[106]
Er:CaF_2	Hot forming	η_{sl} = 3%, P_E = 0.48 mJ	[122]
Tm:CaF_2	Hot forming	η_{sl} = 5.5%, P ≈ 11 mW, CW	[121]

and slope efficiency than single crystals do. They have rarely been reported to be applicable in high-power and ultrashort pulse lasers. Furthermore, compared with fluoride single-crystal materials, the optical quality of fluoride ceramics still needs optimization. The sharp decrease in transmittance at short wavelengths leads to severe optical losses, hindering the realization of higher power output. Future studies should prioritize optimizing the optical quality of ceramic samples, reducing preparation costs, increasing productivity, and ensuring the reproducibility of fabrication processes. Furthermore, research on eliminating defects in fluoride ceramics to enhance material performance is inadequate and warrants further investigation. Table 5 summarizes the common defects in fluoride ceramics along with the proposed solutions for their elimination. Moreover, the range of laser ceramics that utilize not only new hosts such as BaF_2 but also other laser transitions and ions should be further explored.

Table 5 Common defects in fluoride ceramics and solutions for elimination

Defect type	Cause	Elimination solution
Porosity	Incomplete densification	Optimizing the sintering process, addition of sintering additives, and HIP posttreatment
Impurity	Raw material contaminants introduced in the preparation process	Purification of raw materials and controlling the introduction of impurities during preparation
Secondary phase	Easily hydrolyzed fluoride	Sintering in an inert or reducing atmosphere
Cluster	Rare earth ion aggregation	Breaking up clusters by codoping
Internal stress	Formatted during fabrication and process	Optimizing the sintering and processing processes; annealing to remove stress

Acknowledgements

This work was supported by the National Key R&D Program of China (No. 2023YFB3812000), the International Partnership Program of the Chinese Academy of Sciences (No. 121631KYSB20200039), the National Center for Research and Development (No. WPC2/1/SCAPOL/2021), and the Chinese Academy of Sciences President's International Fellowship Initiative (No. 2024VEA0014).

Declaration of competing interest

The authors have no competing interests to declare that are relevant to the content of this article. The author Jiang Li is the Editorial Committee member of this journal. The author Dariusz Hreniak is the Advisory Committee member of this journal.

References

[1] Shen YX, Fu XP, Yao C, *et al.* Optical crystals for 1.3 μm all-solid-state passively Q-switched laser. *Crystals* 2022, **12**: 1060.

[2] Kang PQ, Zhang S, Zhang XL, *et al.* High power self-Q-switched Tm:YAP solid state laser based on the ground state reabsorption. *Infrared Phys Techn* 2022, **123**: 104117.

[3] Shen JP, Lu P, Xu SC, *et al.* First demonstration of watt-level LED-pumped actively Q-switched Nd:glass rod laser. *Appl Phys B-Lasers O* 2024, **130**: 69.

[4] Su XC, Wang YR, Yin YR, *et al.* Sub-100-fs Kerr-lens mode-locked Yb:Lu_2O_3 laser with more than 60% optical efficiency. *Opt Lett* 2024, **49**: 145–148.

[5] Zong MY, Zhang Z, Liu JJ, *et al.* All-solid-state 3-μm single-frequency Er:CaF_2 laser with a stable and switchable wavelength. *Opt Lett* 2024, **49**: 1786–1789.

[6] Asshauer T, Latz C, Mirshahi A, *et al.* Femtosecond lasers for eye surgery applications: Historical overview and modern low pulse energy concepts. *Adv Opt Technol* 2021, **10**: 393–408.

[7] Chen JM, Jiang YE, Wang X, *et al.* High-stability, high-power diode-pumped mode-locked laser with a novel Nd:glass. *Opt Commun* 2024, **558**: 130380.

[8] Guo FF, Rong WL, Chen LJ, *et al.* Novel laser crystal Nd:$LiY(MoO_4)_2$: Crystal growth, characterization, and orthogonally polarized dual-wavelength laser. *Cryst Growth Des* 2024, **24**: 1421–1428.

[9] Zhao CC, Zhang PX, Li SM, *et al.* Development of rare-earth ion doped fluoride laser crystal. *J Synth Cryst* 2022, **51**: 1573–1587. (in Chinese)

[10] Ikesue A, Kinoshita T, Kamata K, *et al.* Fabrication and optical properties of high-performance polycrystalline Nd:YAG ceramics for solid-state lasers. *J Am Ceram Soc* 1995, **78**: 1033–1040.

[11] Guo LH, Shi Y, Tian F, *et al.* Microstructure and laser performance of fine-grained Yb:CaF_2 transparent ceramics prepared by two-step sintering. *Opt Mater* 2023, **140**: 113841.

[12] Liu Q, Wang WL, Dai ZF, *et al.* Fabrication and long persistent luminescence of Ce^{3+}–Cr^{3+} co-doped yttrium aluminum gallium garnet transparent ceramics. *J Rare Earth* 2022, **40**: 1699–1705.

[13] Feng SW, Guo YC, Sun XM, *et al.* Elevating photoluminescence properties of $Y_3MgAl_3SiO_{12}$:Ce^{3+} transparent ceramics for high-power white lighting. *J Rare Earth* 2023, **41**: 649–657.

[14] Zhang YQ, Zhou ZW, Mei BC. Efficient energy transfer of Ce to Nd in SrF_2 transparent ceramics for enhancing NIR emission. *J Eur Ceram Soc* 2023, **43**: 7076–7084.

[15] Chen JM, Mei BC, Li WW, *et al.* Fabrication and spectral performance of Nd_x:$(La_{0.05}Lu_{0.05}Gd_{0.05}Y_{0.05})Ca_{0.8-x}F_{2.2+x}$ high-entropy transparent fluoride ceramics. *Ceram Int* 2024, **50**: 6128–6134.

[16] Chen PH, Li XY, Tian F, *et al.* Fabrication, microstructure, and properties of 8 mol% yttria-stabilized zirconia (8YSZ) transparent ceramics. *J Adv Ceram* 2022, **11**: 1153–1162.

[17] Zhang LX, Hu DJ, Snetkov IL, *et al.* A review on magneto–optical ceramics for Faraday isolators. *J Adv Ceram* 2023, **12**: 873–915.

[18] Jin XH, Dong MJ, Kan YM, *et al.* Fabrication of transparent AlON by gel casting and pressureless sintering. *J Inorg Mater* 2023, **38**: 193–198.

[19] Li WJ, Wang H, Tu BT, *et al.* Preparation and property of $Mg_{0.9}Al_{2.08}O_{3.73}N_{0.03}$ transparent ceramic with broad optical transmission range. *J Inorg Mater* 2022, **37**: 969.

[20] Zhu DY, Nikl M, Chewpraditkul W, *et al.* Development and prospects of garnet ceramic scintillators: A review. *J Adv Ceram* 2022, **11**: 1825–1848.

[21] Liu B, Sha K, Zhou QW, *et al.* One-step cold sintering process towards translucent BaF_2 ceramics. *J Eur Ceram Soc* 2023, **43**: 7053–7058.

[22] Liu ZD, Cao Y, Wang JS, *et al.* Energy transfer and color tunable up-conversion luminescence in PrF_3 and YbF_3 co-doped SrF_2 transparent ceramics. *J Lumin* 2023, **263**: 120064.

[23] Yasyrkina DS, Ermakova JA, Ivanov VK, *et al.* Synthesis of $Ca_{1-x-y}Yb_xEr_yF_{2+x+y}$ upconversion powders for the preparation of optical ceramics. *J Struct Chem+* 2023, **64**: 1733–1742.

[24] Račiukaitis G. Ultra-short pulse lasers for microfabrication: A review. *IEEE J Sel Top Quant* 2021, **27**: 1–12.

[25] Kravtsov NV. Basic trends in the development of diode-pumped solid-state lasers. *Quantum Electron* 2001, **31**: 661–677.
[26] Tikhonchuk VT, Gong T, Jourdain N, *et al.* Studies of laser-plasma interaction physics with low-density targets for direct-drive inertial confinement fusion on the Shenguang III prototype. *Matter Radiat Extremes* 2021, **6**: 025902.
[27] Byer RL. Diode laser-pumped solid-state lasers. *Science* 1988, **239**: 742–747.
[28] Zhao F, Li Y, Meng ZD. Successful treatment of hyperpigmentation from fixed drug eruption with a low-dose and large-spot Q-switched 1064 nm Nd:YAG laser. *J Cosmet Dermatol-US* 2023, **22**: 2128–2130.
[29] Hönninger C, Paschotta R, Graf M, *et al.* Ultrafast ytterbium-doped bulk lasers and laser amplifiers. *Appl Phys B* 1999, **69**: 3–17.
[30] Dong J, Xu GZ, Ma J, *et al.* Investigation of continuous-wave and Q-switched microchip laser characteristics of Yb:YAG ceramics and crystals. *Opt Mater* 2012, **34**: 959–964.
[31] Xu MM, Fang YH, Hu M, *et al.* Exploring the effect of transverse patterns on the temporal characteristics in self-mode-locked Nd:YVO_4 lasers. *Opt Commun* 2022: 129119.
[32] Ji YY, Hu M, Xv MM, *et al.* Exploring the spatial hole burning effect on the mode-locking characteristics of self-mode-locked Nd:YVO_4 lasers. *Opt Commun* 2023, **549**: 129883.
[33] Fan L, Sun R, Wang LM, *et al.* High-power and efficient orthogonally-polarized dual-wavelength Nd:YLF laser. *Laser Phys* 2022, **32**: 125001.
[34] Ma QL, Mo HD, Zhao J. High-energy high-efficiency Nd:YLF laser end-pump by 808 nm diode. *Opt Commun* 2018, **413**: 220–223.
[35] Jouini A, Brenier A, Guyot Y, *et al.* Spectroscopic and laser properties of the near-infrared tunable laser material Yb^{3+}-doped CaF_2 crystal. *Cryst Growth Des* 2008, **8**: 808–811.
[36] Machinet G, Andriukaitis G, Sévillano P, *et al.* High-gain amplification in Yb:CaF_2 crystals pumped by a high-brightness Yb-doped 976 nm fiber laser. *Appl Phys B* 2013, **111**: 495–500.
[37] Ma JS, Pan JX, Wang J, *et al.* High signal-noise ratio passively mode-locked femtosecond Yb:CaF_2 laser at 1034 nm. *Optik* 2021, **241**: 166330.
[38] Wang SZ, Jiang DP, Wu QH, *et al.* Spectral properties and highly efficient continuous-wave laser operation in Nd,Gd:CaF_2 crystals. *J Alloys Compd* 2019, **781**: 629–632.
[39] Liu J, Liu JF, Su LB, *et al.* Effects of Gd^{3+}/Y^{3+} codoping on the spectral properties of Nd:CaF_2 crystals. *Acta Phys Sin* 2016, **65**: 054207. (in Chinese)
[40] Zou ZT, He YF, Yu H, *et al.* Photoluminescence property and laser performance in Yb-doped $Sr_{1-x}Gd_xF_{2+x}$ single crystals. *Opt Mater Express* 2018, **8**: 1747–1753.
[41] Wu YJ, Zou ZT, Wang C, *et al.* Broadly tunable and passively mode-locked operations of Yb^{3+},Gd^{3+}:SrF_2 laser. *IEEE J Sel Top Quant* 2019, **25**: 1100405.
[42] Zhao MF, Wang C, Hao QQ, *et al.* High single-pulse energy passively Q-switched laser based on Yb,Gd:SrF_2 crystal. *Chin Opt Lett* 2020, **18**: 101401.
[43] Agnesi A, Greborio A, Pirzio F, *et al.* 80-fs Nd:silicate glass laser pumped by a single-mode 200-mW diode. *Opt Express* 2010, **18**: 10098–10103.
[44] Brauch U, Röcker C, Graf T, *et al.* High-power, high-brightness solid-state laser architectures and their characteristics. *Appl Phys B* 2022, **128**: 58.
[45] Li DW, Wang T, Yin XL, *et al.* Bandwidth expansion and pulse shape optimized for 10 PW laser design via spectral shaping. *Chin Phys B* 2022, **31**: 094210.
[46] Yang XL, Wang WC, Zhang QY. BaF_2 modified Cr^{3+}/Ho^{3+} co-doped germanate glass for efficient 2.0 μm fiber lasers. *J Non-Cryst Solids* 2018, **482**: 147–153.
[47] Huang SJ, Xiao YB, Liu JL, *et al.* Nd^{3+}-doped antimony germanate glass for 1.06 μm fiber lasers. *J Non-Cryst Solids* 2019, **518**: 10–17.
[48] Khalid M, Chen GY, Bei J, *et al.* Microchip and ultra-fast laser inscribed waveguide lasers in Yb^{3+}germanate glass. *Opt Mater Express* 2019, **9**: 3557.
[49] Ding N, Diao JL, Zhang DW, *et al.* Spectroscopic properties of Yb^{3+} and Nd^{3+} co-doped tellurite glass for 1.0 μm laser application. *Ceram Int* 2020, **46**: 25633–25637.
[50] Denker BI, Dorofeev VV, Galagan BI, *et al.* A 200 mW, 2.3 μm Tm^{3+}-doped tellurite glass fiber laser. *Laser Phys Lett* 2020, **17**: 095101.
[51] Liu JL, Wang WC, Xiao YB, *et al.* Nd^{3+}-doped TeO_2–MoO_3–ZnO tellurite glass for a diode-pump 1.06 μm laser. *J Non Cryst Solids* 2019, **506**: 32–38.
[52] Li SS, Wang YL, Lu ZW, *et al.* Hundred-Joule-level, nanosecond-pulse Nd:glass laser system with high spatiotemporal beam quality. *High Pow Laser Sci Eng* 2016, **4**: e10.
[53] Ji SZ, Huang WF, Wang JF, *et al.* LD end-pumped Joule-level square-rod Nd:glass laser amplifier with high efficiency. *Opt Laser Technol* 2021, **135**: 106634.
[54] Gong L, Zhang H, Qian ZL, *et al.* Generation of 1.8-W average power from a diode-pumped femtosecond rotary Nd:glass disk laser. *IEEE Photonics J* 2020, **12**: 7906811.
[55] Dorrer C, Consentino A, Cuffney R, *et al.* Spectrally tunable, temporally shaped parametric front end to seed high-energy Nd:glass laser systems. *Opt Express* 2017, **25**: 26802–26814.
[56] Dong JS, Wang QG, Xu J, *et al.* Growth and spectral properties of Ho,Y:CaF_2 crystal grown with porous crucible TGT method. *J Synth Cryst* 2022, **51**: 200–207. (in Chinese)
[57] Hao Q, Li WX, Pan HF, *et al.* Laser-diode pumped 40-W Yb:YAG ceramic laser. *Opt Express* 2009, **17**: 17734–17738.
[58] Ikesue A, Aung YL. Ceramic laser materials. *Nat Photonics* 2008, **2**: 721–727.
[59] Taira T. Ceramic YAG lasers. *C R Phys* 2007, **8**: 138–152.
[60] Rao H, Liu ZJ, Cong ZH, *et al.* High power YAG/Nd:YAG/YAG ceramic planar waveguide laser. *Laser Phys Lett* 2017, **14**: 045801.
[61] Kemp A, Valentine G, Burns D. Progress towards high-power, high-brightness neodymium-based thin-disk lasers. *Prog Quant Electron* 2004, **28**: 305–344.
[62] Zhang LX, Li XY, Hu DJ, *et al.* Fabrication and properties of non-stoichiometric $Tb_2(Hf_{1-x}Tb_x)_2O_{7-x}$ magneto-optical ceramics. *J Adv Ceram* 2022, **11**: 784–793.
[63] Wang DW, Wang JP, Yuan HC, *et al.* Metre-scale $Y_3Al_5O_{12}$ (YAG) transparent ceramics by vacuum reactive sintering. *J Inorg Mater* 2023, **38**: 1483.
[64] Yasuhara R, Kawashima T, Sekine T, *et al.* 213 W average power of 2.4 GW pulsed thermally controlled Nd:glass zigzag slab laser with a stimulated Brillouin scattering mirror. *Opt Lett* 2008, **33**: 1711–1713.
[65] Uehara H, Tokita S, Kawanaka J, *et al.* Optimization of laser emission at 2.8 μm by Er:Lu_2O_3 ceramics. *Opt Express* 2018, **26**: 3497–3507.
[66] Lucca A, Jacquemet M, Druon F, *et al.* High-power tunable diode-pumped Yb^{3+}:CaF_2 laser. *Opt Lett* 2004, **29**: 1879–1881.
[67] Kitajima S, Yamakado K, Shirakawa A, *et al.* Yb^{3+}-doped CaF_2–LaF_3 ceramics laser. *Opt Lett* 2017, **42**: 1724–1727.
[68] Hatch SE, Parsons WF, Weagley RJ. Hot-pressed polycrystalline CaF_2:Dy^{2+} laser. *Appl Phys Lett* 1964, **5**: 153–154.
[69] Ikesue A, Yoshida K. Influence of pore volume on laser performance of Nd:YAG ceramics. *J Mater Sci* 1999, **34**: 1189–1195.
[70] Ikesue A, Yoshida K. Scattering in polycrystalline Nd:YAG lasers. *J Am Ceram Soc* 1998, **81**: 2194–2196.
[71] Ikesue A, Yoshida K, Yamamoto T, *et al.* Optical scattering centers in polycrystalline Nd:YAG laser. *J Am Ceram Soc* 1997, **80**: 1517–1522.
[72] Ikesue A, Taira T, Sato Y, *et al.* High-performance microchip lasers using polycrystalline Nd: YAG ceramics. *J Ceram Soc JPN* 2000, **108**: 428–430.
[73] Ikesue A, Kamata K, Yoshida K. Effects of neodymium concentration on optical characteristics of polycrystalline Nd:YAG laser materials. *J Am Ceram Soc* 1996, **79**: 1921–1926.
[74] Takakimi Y, Hideki Y, Hiroo Y. Production of fine powder of yttrium aluminum garnet. JP Patent 10101411A, 1998.

[75] Takakimi Y, Hideki Y, Moriteru I. Production of fine powdery staring material for yttrium aluminum garnet. JP Patent 10101334, 1998.
[76] Tokio K, Hideki Y, Moriteru I. Production of yttrium aluminum garnet fine powder. JP Patent 10101333, 1998.
[77] Lu JR, Prabhu M, Song J, *et al.* Optical properties and highly efficient laser oscillation of Nd: YAG ceramics. *Appl Phys B* 2000, **71**: 469–473.
[78] Lu JR, Ueda KI, Yagi H, *et al.* Neodymium doped yttrium aluminum garnet ($Y_3Al_5O_{12}$) nanocrystalline ceramics—A new generation of solid state laser and optical materials. *J Alloys Compd* 2002, **341**: 220–225.
[79] Lu JR, Murai T, Takaichi K, *et al.* 72 W Nd:$Y_3Al_5O_{12}$ ceramic laser. *Appl Phys Lett* 2001, **78**: 3586–3588.
[80] Lu JR, Song J, Prabhu M, *et al.* High-power Nd:$Y_3Al_5O_{12}$ ceramic laser. *Jpn J Appl Phys* 2000, **39**: L1048.
[81] Yamamoto RM, Bhachu BS, Cutter KP, *et al.* The use of large transparent ceramics in a high powered, diode pumped solid-state laser. In: *Advanced Solid-State Photonics*. California: Optica Publishing Group, 2008: WC5.
[82] Mandl A, Klimek DE. Textron's J-HPSSL 100 kW ThinZag Laser Program. In: Proceedings of the CLEO/QELS: 2010 Laser Science to Photonic Applications, California, USA, 2010: 16–21.
[83] Marmo J, Injeyan H, Komine H, *et al.* Joint high power solid state laser program advancements at Northrop Grumman. In: Proceedings of SPIE-The International Society for Optical Engineering, California, USA, 2009: 719507.
[84] Li Q, Wang Y, Wang J, *et al.* High transparency Pr:Y_2O_3 ceramics: A promising gain medium for red emission solid-state lasers. *J Adv Ceram* 2022, **11**: 874–881.
[85] Yang CL, Huang JQ, Huang QF, *et al.* Optical, thermal, and mechanical properties of $(Y_{1-x}Sc_x)_2O_3$ transparent ceramics. *J Adv Ceram* 2022, **11**: 901–911.
[86] Liu Y, Qin XP, Gan L, *et al.* Preparation of sub-micron spherical Y_2O_3 particles and transparent ceramics. *J Inorg Mater* 2024, **39**: 691–696.
[87] Liu XQ, Jing W, Hao QQ, *et al.* Characterisation of passively Q-switched Yb:Lu_2O_3 ceramic laser based on graphdiyne absorber. *Infrared Phys Techn* 2021, **115**: 103739.
[88] Lu JR, Lu JH, Murai T, *et al.* Nd^{3+}:Y_2O_3 ceramic laser. *Jpn J Appl Phys* 2001, **40**: L1277.
[89] Lu JR, Takaichi K, Uematsu T, *et al.* Yb^{3+}:Y_2O_3 ceramics—A novel solid-state laser material. *Jpn J Appl Phys* 2002, **41**: L1373–L1375.
[90] Xu CW, Yang CD, Zhang H, *et al.* Efficient laser operation based on transparent Nd:Lu_2O_3 ceramic fabricated by spark plasma sintering. *Opt Express* 2016, **24**: 20571–20579.
[91] Klopp P, Petrov V, Griebner U, *et al.* Highly efficient mode-locked Yb:Sc_2O_3 laser. *Opt Lett* 2004, **29**: 391–393.
[92] Toci G, Hostaša J, Patrizi B, *et al.* Fabrication and laser performances of Yb:Sc_2O_3 transparent ceramics from different combination of vacuum sintering and hot isostatic pressing conditions. *J Eur Ceram Soc* 2020, **40**: 881–886.
[93] Dai ZF, Liu Q, Toci G, *et al.* Fabrication and laser oscillation of Yb:Sc_2O_3 transparent ceramics from co-precipitated nano-powders. *J Eur Ceram Soc* 2018, **38**: 1632–1638.
[94] Liu ZY, Toci G, Pirri A, *et al.* Fabrication, microstructures, and optical properties of Yb:Lu_2O_3 laser ceramics from co-precipitated nano-powders. *J Adv Ceram* 2020, **9**: 674–682.
[95] Esser S, Xu XD, Wang J, *et al.* Single-crystal and ceramic Yb:Lu_2O_3 gain media for thin-disk oscillators. *Appl Phys B* 2023, **129**: 160.
[96] Esser S, Röhrer C, Xu XD, *et al.* Ceramic Yb: Lu_2O_3 thin-disk laser oscillator delivering an average power exceeding 1 kW in continuous-wave operation. *Opt Lett* 2021, **46**: 6063–6066.
[97] Tokurakawa M, Shirakawa A, Ueda KI, *et al.* Diode-pumped ultrashort-pulse generation based on Yb^{3+}:Sc_2O_3 and Yb^{3+}:Y_2O_3 ceramic multi-gain-media oscillator. *Opt Express* 2009, **17**: 3353–3361.
[98] Tokurakawa M, Shirakawa A, Ueda KI, *et al.* Diode-pumped sub-100 fs Kerr-lens mode-locked Yb^{3+}:Sc_2O_3 ceramic laser. *Opt Lett* 2007, **32**: 3382–3384.
[99] Paradis C, Modsching N, Wittwer VJ, *et al.* Generation of 35-fs pulses from a Kerr lens mode-locked Yb:Lu_2O_3 thin-disk laser. *Opt Express* 2017, **25**: 14918–14925.
[100] Hostaša J. Ceramics for Laser Technologies. In: *Encyclopedia of Materials: Technical Ceramics and Glasses*. Pomeroy M, Eds. Oxford: Elsevier, 2021: 110–124.
[101] Basiev TT, Doroshenko ME, Konyushkin VA, *et al.* SrF_2:Nd^{3+} laser fluoride ceramics. *Opt Lett* 2010, **35**: 4009–4011.
[102] Liu ZY, Ikesue A, Li J. Research progress and prospects of rare-earth doped sesquioxide laser ceramics. *J Eur Ceram Soc* 2021, **41**: 3895–3910.
[103] Cardinali V, Marmois E, Le Garrec B, *et al.* Determination of the thermo–optic coefficient dn/dT of ytterbium doped ceramics (Sc_2O_3, Y_2O_3, Lu_2O_3, YAG), crystals (YAG, CaF_2) and neodymium doped phosphate glass at cryogenic temperature. *Opt Mater* 2012, **34**: 990–994.
[104] Kuznetsov SV, Alexandrov AA, Fedorov PP. Optical fluoride nanoceramics. *Inorg Mater* 2021, **57**: 555–578.
[105] Basiev TT, Doroshenko ME, Fedorov PP, *et al.* Efficient laser based on CaF_2–SrF_2–YbF_3 nanoceramics. *Opt Lett* 2008, **33**: 521–523.
[106] Basiev TT, Konyushkin VA, Konyushkin DV, *et al.* First ceramic laser in the visible spectral range. *Opt Mater Express* 2011, **1**: 1511–1514.
[107] Jiang YG, Jiang BX, Zhang PD, *et al.* Transparent Nd-doped $Ca_{1-x}Y_xF_{2+x}$ ceramics prepared by the ceramization of single crystals. *Mater Design* 2017, **113**: 326–330.
[108] Aubry P, Bensalah A, Gredin P, *et al.* Synthesis and optical characterizations of Yb-doped CaF_2 ceramics. *Opt Mater* 2009, **31**: 750–753.
[109] Mortier M, Lyberis A, Suganuma A, *et al.* Last advances in Yb^{3+} doped CaF_2 ceramics synthesis. In: *Solid State Lasers XX: Technology and Devices*. Clarkson W A, Hodgson N, Shori R, Eds. California, USA, 2011: 7912R.
[110] Jiang YG, Jiang BX, Jiang N, *et al.* Heat-driven tailored for eliminating Nd^{3+} re-clusters in Nd^{3+},Gd^{3+}-codoped SrF_2 laser ceramic. *J Am Ceram Soc* 2020, **103**: 2562–2568.
[111] Basiev TT, Doroshenko ME, Konyushkin VA, *et al.* Lasing in diode-pumped fluoride nanostructure F_2^-:LiF colour centre ceramics. *Quantum Electron+* 2007, **37**: 989–990.
[112] Sherry WM, Sande JBV. Microstructural characterization of calcium flouride single crystals deformed in steady state. *J Mater Sci* 1981, **16**: 1477–1489.
[113] Reppich B. Inhomogeneous dislocation distributions and the formation of dislocation cell structure. *J Mater Sci* 1971, **6**: 267–269.
[114] Basiev TT, Demidenko VA, Dykel'skii KV, *et al.* Optical fluoride and oxysulphide ceramics preparation and characterization. In: *Developments in Ceramic Materials Research*. Dena R, Ed. New York: Nova Science Publishers, Inc., 2007: 53–95.
[115] Alimov OK, Basiev TT, Doroshenko ME, *et al.* Spectroscopic and oscillation properties of Yb^{3+} ions in BaF_2–SrF_2–CaF_2 crystals and ceramics. In: *Advanced Solid-State Photonics*. California: Optica Publishing Group, 2009: WB25.
[116] Akchurin MS, Basiev TT, Demidenko AA, *et al.* CaF_2:Yb laser ceramics. *Opt Mater* 2013, **35**: 444–450.
[117] Popov PA, Dukel'skiĭ KV, Mironov IA, *et al.* Thermal conductivity of CaF_2 optical ceramic. *Dokl Phys* 2007, **52**: 7–9.
[118] Basiev TT, Voronov VV, Konyushkin VA, *et al.* Optical lithium fluoride ceramics. *Dokl Phys* 2007, **52**: 677–680.
[119] Bol'shchikov FA, Garibin EA, Gusev PE, *et al.* Nanostructured Tm: CaF_2 ceramics: Potential gain media for two micron lasers. *Quantum Electron* 2011, **41**: 193–197.
[120] Lyapin AA, Fedorov PP, Garibin EA, *et al.* Spectroscopic, luminescent and laser properties of nanostructured CaF_2:Tm materials. *Opt Mater* 2013, **35**: 1859–1864.
[121] Ryabochkina PA, Lyapin AA, Osiko VV, *et al.* Structural, spectral-

luminescent, and lasing properties of nanostructured Tm:CaF_2 ceramics. *Quantum Electron* 2012, **42**: 853–857.
[122] Šulc J, Němec M, Švejkar R, *et al.* Diode-pumped Er:CaF_2 ceramic 2.7 μm tunable laser. *Opt Lett* 2013, **38**: 3406–3409.
[123] Jiang YG, Jiang BX, Jiang N, *et al.* Er^{3+}-doped CaF_2 polycrystalline ceramic with perfect transparency for mid-infrared laser. *J Am Ceram Soc* 2020, **103**: 5808–5812.
[124] Kuznetsov SV, Fedorov PP. Morphological stability of solid–liquid interface during melt crystallization of $M_{1-x}R_xF_{2+x}$ solid solutions. *Inorg Mater* 2008, **44**: 1434–1458.
[125] Li J, Pan YB, Zeng YP, *et al.* The history, development, and future prospects for laser ceramics: A review. *Int J Refract Met H* 2013, **39**: 44–52.
[126] Liu XW, Tan GL, Zhou ZW, *et al.* Effect of Pr^{3+} doping concentration on microstructure and optical properties of transparent BaF_2 ceramics. *J Alloys Compd* 2022, **895**: 162623.
[127] Wei JB, Toci G, Pirri A, *et al.* Fabrication and property of Yb:CaF_2 laser ceramics from co-precipitated nanopowders. *J Inorg Mater* 2019, **34**: 1341–1348.
[128] Guo LH, Shi Y, Chen GM, *et al.* Fabrication of sub-micrometer sized Er:CaF_2 transparent ceramics for eye-safe lasers. *Opt Mater* 2022, **133**: 113052.
[129] Liu XW, Zhou ZW, Li WW, *et al.* The effects of the solution reactant concentration and temperature on the preparation of Pr^{3+}:BaF_2 transparent ceramics. *J Am Ceram Soc* 2021, **104**: 3862–3872.
[130] Hu SC, De Jonghe LC. Pre-eutectic densification in MgF_2–CaF_2. *Ceram Int* 1983, **9**: 123–126.
[131] Kong LB, Huang YZ, Que WX, *et al.* Transparent Ceramics. Switzerland: Springer Cham, 2015.
[132] Chen L, Mei BC, Li WW, *et al.* Effect of reactive raw materials and pre-loading pressure on the microstructure and transmittance of pure CaF_2 transparent ceramics. *Mater Chem Phys* 2023, **297**: 127315.
[133] Ermakova YA, Pominova DV, Voronov VV, *et al.* Synthesis of SrF_2:Yb:Er ceramic precursor powder by co-precipitation from aqueous solution with different fluorinating media: NaF, KF and NH_4F. *Dalton T* 2022, **51**: 5448–5456.
[134] Li WW, Huang HJ, Mei BC, *et al.* Synthesis of highly sinterable Yb:SrF_2 nanopowders for transparent ceramics. *Opt Mater* 2018, **75**: 7–12.
[135] Li WW, Huang HJ, Mei BC, *et al.* Comparison of commercial and synthesized CaF_2 powders for preparing transparent ceramics. *Ceram Int* 2017, **43**: 10403–10409.
[136] Ishizawa H. CaF_2 translucent ceramics and manufacturing method of CaF_2 translucent ceramics. US patent 9586867, 2017.
[137] Li WW, Jing W, Mei BC, *et al.* Effect of NaF doping on the transparency, microstructure and spectral properties of Yb^{3+}:CaF_2 transparent ceramics. *J Eur Ceram Soc* 2020, **40**: 4572–4577.
[138] Liu ZD, Shen QL, Fu SC, *et al.* Effects of LiF sintering additive on the microstructure and mechanical properties of hot-pressed CaF_2 transparent ceramics. *Opt Mater X* 2022, **14**: 100147.
[139] Liu ZD, Shen QL, Cao Y, *et al.* Enhanced visible luminescence intensities in hot-pressed Pr, La:SrF_2 transparent ceramics by co-doping with LaF_3. *J Lumin* 2023, **256**: 119652.
[140] Kawano N, Kato T, Nakauchi D, *et al.* Dosimetric and scintillation properties of Tm-doped BaF_2 translucent ceramics. *J Mater Sci Mater El* 2023, **34**: 962.
[141] Kawano N, Kato T, Nakauchi D, *et al.* TSL, OSL and scintillation properties of Tb-doped barium fluoride translucent ceramics. *Opt Mater* 2023, **141**: 113948.
[142] Feng YG, Chen GM, Guo LH, *et al.* Fabrication of Er:SrF_2 transparent ceramics by air pre-sintering and hot isostatic pressing. *Opt Mater* 2023, **142**: 114009.
[143] Li JL, Chen XQ, Tang LF, *et al.* Fabrication and properties of transparent Nd-doped BaF_2 ceramics. *J Am Ceram Soc* 2019, **102**: 178–184.
[144] Chen XQ, Wu YQ. High concentration Ce^{3+} doped BaF_2 transparent ceramics. *J Alloys Compd* 2020, **817**: 153075.
[145] Zhang CH, Yi GQ, Sun ZC, *et al.* Cr^{3+} doped CaF_2 transparent ceramic with effective broadband near-infrared emission. *Mater Lett* 2023, **346**: 134506.
[146] Yi GQ, Liu ZD, Li WW, *et al.* Gd^{3+} doping induced microstructural evolution and enhanced visible luminescence of Pr^{3+} activated calcium fluoride transparent ceramics. *Ceram Int* 2023, **49**: 7333–7340.
[147] Guo NJ, Gong YP, Zhu GS, *et al.* Preparation and properties of 5 at% Er^{3+}:SrF_2 transparent ceramics by cold sintering. *Opt Mater* 2023, **142**: 114073.
[148] Gao J, Xia ZG, Ding Q, *et al.* Cold sintering of highly transparent calcium fluoride nanoceramic as a universal platform for high-power lighting. *Adv Funct Mater* 2023, **33**: 2302088.
[149] Samuel P, Ishizawa H, Ezura Y, *et al.* Spectroscopic analysis of Eu doped transparent CaF_2 ceramics at different concentration. *Opt Mater* 2011, **33**: 735–737.
[150] Song LM, Gao JH, Wang X, *et al.* Highly luminescent Cit/CaF_2:Ce^{3+},Tb^{3+} nanoparticles and detection of Cu^{2+} ions. *J Lumin* 2020, **226**: 117445.
[151] Bensalah A, Mortier M, Patriarche G, *et al.* Synthesis and optical characterizations of undoped and rare-earth-doped CaF_2 nanoparticles. *J Solid State Chem* 2006, **179**: 2636–2644.
[152] Tian Y, Yu JC, Qi XH, *et al.* Bio-conjugation of CaF_2:Eu/chitosan nanoparticles with BSA and photoluminescent properties. *J Mater Sci-Mater El* 2009, **20**: 439–444.
[153] Lian HZ, Liu J, Ye ZR, *et al.* Synthesis and photoluminescence properties of erbium-doped BaF_2 nanoparticles. *Chem Phys Lett* 2004, **386**: 291–294.
[154] Bender CM, Burlitch JM, Barber D, *et al.* Synthesis and fluorescence of neodymium-doped barium fluoride nanoparticles. *Chem Mater* 2000, **12**: 1969–1976.
[155] Abid N, Khan AM, Shujait S, *et al.* Synthesis of nanomaterials using various top–down and bottom–up approaches, influencing factors, advantages, and disadvantages: A review. *Adv Colloid Interfac* 2022, **300**: 102597.
[156] Singh SG, Singh AK, Sen S, *et al.* Synthesis and luminescence studies of Mn doped CaF_2. In: *International Conference on Physics of Emerging Functional Materials (PEFM-2010)*. Aswal DK, Debnath AK, Eds. Mumbai: AIP Publishing, 2010: 340–342.
[157] Zhi GL, Song JH, Mei BC, *et al.* Synthesis and characterization of Er^{3+} doped CaF_2 nanoparticles. *J Alloys Compd* 2011, **509**: 9133–9137.
[158] Sen S, Singh SG, Patra GD, *et al.* Synthesis of optically transparent ceramic of CaF_2 doped with Mn and Ce for thermoluminescent dosimetry. In: *Solid State Physics*. Mukhopadhyay R, Ed. USA: American Institute of Physics, 2012: 279–280.
[159] Singh SG, Sen S, Patra GD, *et al.* Fabrication, properties and thermo–luminescent dosimetric application of CaF_2:Mn transparent ceramic. *Nucl Instrum Meth B* 2012, **287**: 51–55.
[160] Li WW, Mei BC, Li XN, *et al.* Effects of Na^+ on spectral properties of Er^{3+}:CaF_2 transparent ceramic. *Key Eng Mater* 2013, **531–532**: 307–311.
[161] Sen S, Mittal G, Deshpande SK, *et al.* Effect of porosity on Impedance of CaF_2 ceramic. In: *Solid State Physics*. Chauhan A K, Murli C, Gadkari S C, Eds. USA: American Institute of Physics, 2013: 936–937.
[162] Liu ZD, Mei BC, Song JH, *et al.* Fabrication and optical characterizations of Yb, Er codoped CaF_2 transparent ceramic. *J Eur Ceram Soc* 2014, **34**: 4389–4394.
[163] Zhou WB, Cai FF, Zhi GL, *et al.* Fabrication of highly-transparent Er:CaF_2 ceramics by hot-pressing technique. *Mater Sci-Poland* 2014, **32**: 358–363.
[164] Liu ZD, Mei BC, Song JH, *et al.* Microstructure and optical properties of hot-pressed Er:CaF_2 transparent ceramics. *J Alloys Compd* 2015, **646**: 760–765.
[165] Singh SG, Sen S, Patra GD, *et al.* Luminescence properties of CaF_2:Mn optically transparent ceramic. *J Lumin* 2015, **166**: 222–226.

[166] Li WW, Mei BC, Song JH, *et al.* Yb^{3+} doped CaF_2 transparent ceramics by spark plasma sintering. *J Alloys Compd* 2016, **660**: 370–374.
[167] Liu XY, Mei BC, Li WW, *et al.* Effect of sintering temperature on the microstructure and transparency of Nd,Y:CaF_2 ceramics. *Ceram Int* 2016, **42**: 13285–13290.
[168] Sarthou J, Aballéa P, Patriarche G, *et al.* Wet-route synthesis and characterization of Yb:CaF_2 optical ceramics. *J Am Ceram Soc* 2016, **99**: 1992–2000.
[169] Sun ZC, Mei BC, Li WW, *et al.* Synthesis and optical characterizations of Nd,Y:CaF_2 transparent ceramics. *Opt Mater* 2017, **71**: 35–40.
[170] Xiong F, Song JH, Li WW, *et al.* Influence of sintering conditions on the microstructure and optical properties of Eu:CaF_2 transparent ceramic. *Mater Res Bull* 2017, **95**: 138–145.
[171] Kuznetsov SV, Morozov OA, Gorieva VG, *et al.* Synthesis and luminescence studies of CaF_2:Yb:Pr solid solutions powders for photonics. *J Fluorine Chem* 2018, **211**: 70–75.
[172] Liu L, Song JH, Li WW, *et al.* Effect of sintering temperature on the microstructure and optical properties of Mn:CaF_2 transparent ceramics. *Mater Chem Phys* 2018, **204**: 345–349.
[173] Xie XY, Mei BC, Song JH, *et al.* Fabrication and spectral properties of Nd,La:CaF_2 transparent ceramics. *Opt Mater* 2018, **76**: 111–116.
[174] Yi GQ, Li WW, Song JH, *et al.* Structural, spectroscopic and thermal properties of hot-pressed Nd:$(Ca_{0.94}Gd_{0.06})F_{2.06}$ transparent ceramics. *J Eur Ceram Soc* 2018, **38**: 3240–3245.
[175] Yi GQ, Li WW, Song JH, *et al.* The effect of Gd^{3+} ions on fabrication and luminescence properties of Nd^{3+}-doped $(Ca_{1-x}Gd_x)F_{2+x}$ transparent ceramics. *Mater Res Bull* 2018, **102**: 304–310.
[176] Liu JS, Song JH, Mei BC, *et al.* Fabrication and mid-infrared property of Er:CaF_2 transparent ceramics. *Mater Res Bull* 2019, **111**: 158–164.
[177] Yang Y, Li WW, Mei BC, *et al.* Synthesis and enhanced upconversion luminescence upon two-wavelength excitation of Er^{3+}:CaF_2 transparent ceramics. *J Lumin* 2019, **213**: 504–509.
[178] Yi GQ, Li WW, Song JH, *et al.* Preparation and characterizations of Pr^{3+}:CaF_2 transparent ceramics with different doping concentrations. *Ceram Int* 2019, **45**: 3541–3546.
[179] Zhou ZW, Li WW, Song JH, *et al.* Application of Judd–Ofelt theory in analyzing Nd^{3+} doped SrF_2 and CaF_2 transparent ceramics. *J Eur Ceram Soc* 2019, **39**: 2446–2452.
[180] Zhou ZW, Mei BC, Song JH, *et al.* Effects of Sr^{2+} content on microstructure and spectroscopic properties of Nd^{3+} doped $Ca_{1-x}Sr_xF_2$ transparent ceramics. *J Alloys Compd* 2019, **811**: 152046.
[181] Li WW, Huang HJ, Mei BC, *et al.* Effect of Yb concentration on the microstructures, spectra, and laser performance of Yb:CaF_2 transparent ceramics. *J Am Ceram Soc* 2020, **103**: 5787–5795.
[182] Li WW, Huang HJ, Mei BC, *et al.* Fabrication, microstructure and laser performance of Yb^{3+} doped CaF_2–YF_3 transparent ceramics. *Ceram Int* 2020, **46**: 19530–19536.
[183] Liu Q, Liu Y, Wei JB, *et al.* Preparation and properties of Yb:CaF_2 transparent ceramics. *J Synth Cryst* 2020, **49**: 799–803. (in Chinese)
[184] Huang XY, Chen GM, Wei JB, *et al.* Fabrication of Yb, La:CaF_2 transparent ceramics by air pre-sintering with hot isostatic pressing. *Opt Mater* 2021, **116**: 111108.
[185] Ling HR, Mei BC, Li WW, *et al.* Synthesis and optical characterizations of Yb^{3+}:$Ca_xSr_{1-x}F_2$ transparent ceramics. *Crystals* 2021, **11**: 652.
[186] Yang Y, Zhou ZW, Mei BC, *et al.* Fabrication and upconversion luminescence properties of Er:SrF_2 transparent ceramics compared with Er:CaF_2. *Ceram Int* 2021, **47**: 17139–17146.
[187] Fan XL, Fan JT, Qian KC, *et al.* Preparation of MgF_2–CaF_2 nanocomposite ceramics with high infrared transmittance. *J Eur Ceram Soc* 2022, **42**: 7203–7208.
[188] Guo NJ, Zhu GS, Xu HR, *et al.* Preparation of CaF_2 transparent ceramics by cold sintering. *Ceram Int* 2022, **48**: 34184–34189.
[189] Liu ZY, Wei JB, Toci G, *et al.* Microstructure and laser emission of Yb:CaF_2 transparent ceramics fabricated by air pre-sintering and hot isostatic pressing. *Opt Mater* 2022, **129**: 112540.
[190] Zhan CJ, Mei BC, Sun ZC, *et al.* Fabrication and spectroscopic properties of hot-pressed Tb:CaF_2 transparent ceramics with different doping concentrations. *Opt Mater* 2022, **126**: 112128.
[191] Lyberis A, Patriarche G, Gredin P, *et al.* Origin of light scattering in ytterbium doped calcium fluoride transparent ceramic for high power lasers. *J Eur Ceram Soc* 2011, **31**: 1619–1630.
[192] Li X, Hu C, Guo LH, *et al.* Optimization of Yb:CaF_2 transparent ceramics by air pre-sintering and hot isostatic pressing. *Ceramics* 2024, **7**: 1053–1065.
[193] Breuer S, Lunghammer S, Kiesl A, *et al.* F anion dynamics in cation-mixed nanocrystalline LaF_3:SrF_2. *J Mater Sci* 2018, **53**: 13669–13681.
[194] Sorokin NI, Karimov DN, Smirnov AN, *et al.* Effect of heat treatment in a CF_4 atmosphere on the ion-conductive properties of hot-pressed 95 mol% CeF_3 × 5 mol% SrF_2 ceramics. *Crystallogr Rep+* 2019, **64**: 105–109.
[195] Li WW, Mei BC, Song JH, *et al.* Fabrication and optical property of highly transparent SrF_2 ceramic. *Mater Lett* 2015, **159**: 210–212.
[196] Zhu CH, Song JH, Mei BC, *et al.* Fabrication and optical characterizations of CaF_2–SrF_2–NdF_3 transparent ceramic. *Mater Lett* 2016, **167**: 115–117.
[197] Antuzevics A, Kemere M, Krieke G. Multisite formation in gadolinium doped SrF_2 nanoparticles. *J Alloys Compd* 2018, **762**: 500–507.
[198] Liu J, Liu P, Wang J, *et al.* Fabrication and sintering behavior of Er:SrF_2 transparent ceramics using chemically derived powder. *Materials* 2018, **11**: 475.
[199] Lyapin AA, Ryabochkina PA, Gushchin SV, *et al.* Upconversion luminescence of fluoride phosphors SrF_2:Er,Yb under laser excitation at 1.5 μm. *Opt Spectrosc* 2018, **125**: 537–542.
[200] Zhou ZW, Li WW, Song JH, *et al.* Synthesis and characterization of Nd^{3+} doped SrF_2 nanoparticles prepared by precipitation method. *Ceram Int* 2018, **44**: 4344–4350.
[201] Qin SY, Song JH, Wang WX, *et al.* Study in optical and mechanical properties of Nd^{3+},Y^{3+}:SrF_2 transparent ceramics prepared by hot-pressing and hot-forming techniques. *Crystals* 2019, **9**: 619.
[202] Yi GQ, Mei BC, Li WW, *et al.* Synthesis and luminescence characterization of Pr^{3+},Gd^{3+} co-doped SrF_2 transparent ceramics. *J Am Ceram Soc* 2020, **103**: 279–286.
[203] Zhu T, Mei BC, Li WW, *et al.* Fabrication, microstructure and spectral properties of Nd:SrF_2 transparent ceramics with different concentration of La^{3+} ions. *Opt Mater* 2019, **89**: 598–603.
[204] Gao YW, Mei BC, Li WW, *et al.* Effect of Yb^{3+} concentration on microstructure and optical properties of Yb:SrF_2 transparent ceramics. *Opt Mater* 2020, **105**: 109869.
[205] Krahl T, Beer F, Relling A, *et al.* Toward luminescent composites by phase transfer of SrF_2 : Eu^{3+} nanoparticles capped with hydrophobic antenna ligands. *ChemNanoMat* 2020, **6**: 1086–1095.
[206] Milisavljevic I, Wu YQ, Zych E. The effect of Gd^{3+} doping on luminescence properties of (Gd,Ce):SrF_2 nanopowders and transparent ceramics. *J Lumin* 2020, **224**: 117243.
[207] Yu SQ, Wu YQ. Fabrication, microstructure and optical properties of Ce:SrF_2 transparent ceramics. *Opt Mater* 2020, **105**: 109898.
[208] Liu ZD, Ji YM, Xu CY, *et al.* Microstructural, spectroscopic and mechanical properties of hot-pressed Er:SrF_2 transparent ceramics. *J Eur Ceram Soc* 2021, **41**: 4907–4914.
[209] Liu ZD, Shen QL, Wang YQ, *et al.* Fabrication and optical characterizations of PrF_3-doped SrF_2 transparent ceramics. *Opt Mater* 2021, **122**: 111710.
[210] Liu ZD, Zhang SY, Dong PY, *et al.* Fabrication and optical characterizations of hot-pressed transparent SrF_2/Nd:SrF_2/SrF_2 composite ceramic. *J Eur Ceram Soc* 2021, **41**: 768–774.
[211] Zheng CK, Sun ZC, Li WW, *et al.* Fabrication and spectral properties of Dy:SrF_2 transparent ceramics. *Mater Chem Phys* 2021, **273**: 125141.
[212] Liu ZD, Liu Y, Fu SC, *et al.* Densification and microstructure evolution of hot-pressed Er:SrF_2 transparent ceramics. *Mater Chem Phys* 2022, **278**: 125682.

[213] Ryszczyńska S, Grzyb T. NIR-to-NIR and NIR-to-vis up-conversion of SrF_2:Ho^{3+} nanoparticles under 1156 nm excitation. *Methods Appl Fluores* 2022, **10**: 024001.
[214] Yang Y, Mei BC, Zhou ZW, *et al.* Fabrication and spectroscopic investigations on Er^{3+},Ho^{3+}:SrF_2 transparent ceramics for 2.7 μm emission. *J Eur Ceram Soc* 2022, **42**: 1722–1730.
[215] Zhou ZW, Zhang YQ, Liu XW, *et al.* Effects of Nd^{3+} doping content on microstructure and spectral properties of Nd:SrF_2 transparent ceramic. *J Alloys Compd* 2022, **926**: 166898.
[216] Zhou ZW, Zhang YQ, Zhou LP, *et al.* A novel co-precipitation method to fabricate the high-quality Nd:SrF_2 transparent ceramic. *Mater Lett* 2022, **318**: 132229.
[217] Kuznetsov SV, Ermakova YA, Boldyrev KN, *et al.* Single-phase nanopowders of $Sr_{0.85-x}Ba_xEu_{0.15}F_{2.15}$: Investigation of structure and X-ray luminescent properties. *Ceram Int* 2023, **49**: 39189–39195.
[218] Zhai PF, Mei BC, Song JH, *et al.* Preparation of Ce^{3+}:BaF_2 transparent ceramic by hot-pressed method. *Chin J Lumin* 2012, **33**: 698–706. (in Chinese)
[219] Luo JM, Sahi S, Groza M, *et al.* Luminescence and scintillation properties of BaF_2Ce transparent ceramic. *Opt Mater* 2016, **58**: 353–356.
[220] Luo JM, Ye LF, Xu JL. Preparation and properties of Ce^{3+}:BaF_2 transparent ceramics by vacuum sintering. *J Nanosci Nanotechno* 2016, **16**: 3985–3989.
[221] Kato T, Okada G, Fukuda K, *et al.* Development of BaF_2 transparent ceramics and evaluation of the scintillation properties. *Radiat Meas* 2017, **106**: 140–145.
[222] Khanin V, Venevtsev I, Rodnyi P. Recent advances in the study of core-valence luminescence (cross luminescence). Review. *Opt Mater* 2023, **136**: 113399.
[223] Benemanskaya G, Garibin E, Gusev Y, *et al.* Photosensors for PET scanner on the base of BaF_2 crystals. *Nucl Instrum Meth A* 2009, **610**: 335–337.
[224] Lyberis A, Stevenson AJ, Suganuma A, *et al.* Effect of Yb^{3+} concentration on optical properties of Yb:CaF_2 transparent ceramics. *Opt Mater* 2012, **34**: 965–968.
[225] Jin DH, Liu B, Song KX, *et al.* Boosting densification and microwave dielectric properties in cold sintered BaF_2 ceramics for 5.8 GHz WLAN applications. *J Alloys Compd* 2021, **886**: 161141.
[226] Nakamura F, Kato T, Okada G, *et al.* Scintillation and dosimeter properties of CaF_2 transparent ceramics doped with Nd^{3+} produced by SPS. *J Eur Ceram Soc* 2017, **37**: 4919–4924.
[227] Wang P, Huang ZF, Morita K, *et al.* Transmittance enhancement of spark plasma sintered CaF_2 ceramics by preheating commercial powder. *J Eur Ceram Soc* 2021, **41**: 4609–4617.
[228] Kallel T, Hassairi MA, Dammak M, *et al.* Spectra and energy levels of Yb^{3+} ions in CaF_2 transparent ceramics. *J Alloys Compd* 2014, **584**: 261–268.
[229] Liu XQ, Hao QQ, Liu J, *et al.* Yb:CaF_2–YF_3 transparent ceramics ultrafast laser at dual gain lines. *Chinese Phys B* 2022, **31**: 114205.
[230] Lu G, Mei BC, Song JH, *et al.* Fabrication and properties of highly transparent Nd-doped CaF_2 ceramics. *Mater Lett* 2014, **115**: 162–164.
[231] Sun ZC, Mei BC, Li WW, *et al.* Effects of Nd concentration on microstructure and optical properties of Nd:CaF_2 transparent ceramics. *J Am Ceram Soc* 2016, **99**: 4039–4044.
[232] Liu ZD, Mei BC, Song JH, *et al.* Optical characterizations of hot-pressed erbium-doped calcium fluoride transparent ceramic. *J Am Ceram Soc* 2014, **97**: 2506–2510.
[233] Xing RZ, Mei BC, Song JH, *et al.* Fluorescence and Judd–Ofelt analysis of Er^{3+} doped CaF_2 transparent ceramic. *Adv Mat Res* 2014, **875–877**: 23–27.
[234] Li WW, Liu ZD, Zhou ZW, *et al.* Characterizations of a hot-pressed Er and Y codoped CaF_2 transparent ceramic. *J Eur Ceram Soc* 2016, **36**: 3481–3486.
[235] Liu ZD, Jia MY, Liu X, *et al.* Fabrication and characterizations of hot-pressed Er,Yb:CaF_2 transparent ceramics. *Bull Chin Ceram Soc* 2018, **37**: 2417–2422. (in Chinese)
[236] Liu ZD, Jia MY, Yi GQ, *et al.* Fabrication and microstructure characterizations of transparent Er:CaF_2 composite ceramic. *J Am Ceram Soc* 2019, **102**: 285–293.
[237] Yang Y, Zhou ZW, Mei BC, *et al.* Energy transfer and controllable colors of upconversion emission in Er^{3+} and Dy^{3+} co-doped CaF_2 transparent ceramics. *J Eur Ceram Soc* 2021, **41**: 7835–7844.
[238] Li WW, Huang HJ, Mei BC, *et al.* Fabrication and characterization of polycrystalline Ho:CaF_2 transparent ceramics for 2.0 μm laser application. *Mater Lett* 2017, **207**: 37–40.
[239] Wan ZZ, Li WW, Mei BC, *et al.* Fabrication and spectral properties of Ho-doped calcium fluoride transparent ceramics. *J Lumin* 2020, **223**: 117188.
[240] Ghosh M, Sen S, Pitale SS, *et al.* Growth and optical properties of partially transparent Eu doped CaF_2 ceramic. In: *Solid State Physics Proceedings of the 58th DAE Solid State Physics Symposium*. Murli C, Bhattacharyya D, Gadkari S C, Eds. USA: AIP Publishing LLC, 2014: 592–594.
[241] Ashurov MK, Nuritdinov I, Boiboboeva ST, *et al.* Optical properties of single crystals and nanoceramics of CaF_2–SrF_2–YbF_3 solid solutions. *Inorg Mater* 2022, **58**: 886–892.
[242] Sorokin NI, Karimov DN, Komar'kova ON, *et al.* Effect of heat treatment in HF atmosphere on the optical and electrical properties of BaF_2 ceramics. *Inorg Mater* 2009, **45**: 1188–1192.
[243] Batygov SK, Bolyasnikova LS, Demidenko VA, *et al.* BaF_2:Ce^{3+} scintillation ceramics. *Dokl Phys* 2008, **53**: 485–488.
[244] Demidenko AA, Garibin EA, Gain SD, *et al.* Scintillation parameters of BaF_2 and BaF_2:Ce^{3+} ceramics. *Opt Mater* 2010, **32**: 1291–1293.
[245] Liu YL, Sun Q, Wang DW, *et al.* Development of the cold sintering process and its application in solid-state lithium batteries. *J Power Sources* 2018, **393**: 193–203.
[246] Yu T, Cheng J, Li L, *et al.* Current understanding and applications of the cold sintering process. *Front Chem Sci Eng* 2019, **13**: 654–664.
[247] Liu B, Lin FL, Hu CC, *et al.* Novel transparent LiF ceramics enabled by cold sintering at 150 °C. *Scripta Mater* 2022, **220**: 114917.
[248] Akinribide OJ, Mekgwe GN, Akinwamide SO, *et al.* A review on optical properties and application of transparent ceramics. *J Mater Res Technol* 2022, **21**: 712–738.
[249] Kato T, Nakauchi D, Kawaguchi N, *et al.* Radio-photoluminescence properties of CaF_2 transparent and opaque ceramics. *Curr Appl Phys* 2020, **20**: 1195–1200.
[250] Kato T, Nakauchi D, Kawaguchi N, *et al.* Radio-photoluminescence phenomenon in non-doped CaF_2 ceramic. *Mater Lett* 2020, **270**: 127688.
[251] Nakamura F, Kato T, Okada G, *et al.* Scintillation and dosimeter properties of CaF_2 transparent ceramic doped with Eu^{2+}. *Ceram Int* 2017, **43**: 604–609.
[252] Kato T, Nakauchi D, Kawaguchi N, *et al.* Dy-concentration dependence on dosimetric properties of CaF_2 transparent ceramics. *Opt Mater* 2022, **132**: 112785.
[253] Kawano N, Kato T, Conner RL, *et al.* Radiation response properties of Ce-doped CaF_2 transparent ceramics. *Mater Res Bull* 2024, **171**: 112609.
[254] Kato T, Okada G, Nakauchi D, *et al.* Na-concentration dependence on radiophotoluminescence properties of CaF_2. *Solid State Sci* 2022, **128**: 106892.
[255] Kato T, Nakauchi D, Kawaguchi N, *et al.* Comparative study of optical and dosimetric properties of Mn-doped CaF_2. *Jpn J Appl Phys* 2024, **63**: 01SP05.
[256] Kato T, Nakauchi D, Kawaguchi N, *et al.* Thermally stimulated luminescence properties of transparent ceramics for personal dosimetry. *Jpn J Appl Phys* 2023, **62**: 010604.
[257] Kato T, Nakauchi D, Kawaguchi N, *et al.* Radiophotoluminescence phenomenon of CaF_2 ceramics doped with Li. *Photonics* 2023, **10**: 211.
[258] Kato T, Kawano N, Okada G, *et al.* Scintillation properties of SrF_2 translucent ceramics and crystal. *Optik* 2018, **168**: 956–962.

[259] Kato T, Nakauchi D, Kawaguchi N, *et al.* Scintillation properties of Eu-doped SrF_2 transparent ceramics. *Sensor Mater* 2024, **36**: 531.
[260] Kawano N, Kato T, Conner RL, *et al.* Scintillation and dosimeter properties of Tb-doped strontium fluoride transparent ceramics. *J Lumin* 2024, **276**: 120868.
[261] Nakamura F, Kato T, Okada G, *et al.* Scintillation and storage luminescence properties of MgF_2 transparent ceramics doped with Ce^{3+}. *Opt Mater* 2017, **72**: 470–475.
[262] Nakamura F, Kato T, Okada G, *et al.* Scintillation, dosimeter and optical properties of MgF_2 transparent ceramics doped with Gd^{3+}. *Mater Res Bull* 2018, **98**: 83–88.
[263] Wang P, Yang MJ, Zhang S, *et al.* Suppression of carbon contamination in SPSed CaF_2 transparent ceramics by Mo foil. *J Eur Ceram Soc* 2017, **37**: 4103–4107.
[264] Wang P, Huang ZF, Morita K, *et al.* Influence of spark plasma sintering conditions on microstructure, carbon contamination, and transmittance of CaF_2 ceramics. *J Eur Ceram Soc* 2022, **42**: 245–257.
[265] Popov PA, Fedorov PP, Garibin EA, *et al.* Thermal conductivity of $Ca_{1-x}Ho_xF_{2+x}$ optical ceramics. *Inorg Mater* 2012, **48**: 857–860.
[266] Jiang YG, Jiang BX, Zhu QH, *et al.* Effects of deformation rate on properties of Nd,Y-codoped CaF_2 transparent ceramics. *J Eur Ceram Soc* 2018, **38**: 2404–2409.
[267] Liu ZD, Mei BC, Song JH, *et al.* Influence of Yb concentration on the optical properties of CaF_2 transparent ceramics codoped with Er and Yb. *J Am Ceram Soc* 2015, **98**: 3905–3910.
[268] Li WW, Huang HJ, Mei BC, *et al.* Effect of Y^{3+} ion doping on the microstructure, transmittance and thermal properties of CaF_2 transparent ceramics. *J Alloys Compd* 2018, **747**: 359–365.
[269] Liu ZD, Jia MY, Liu X, *et al.* Fabrication and microstructure characterizations of transparent polycrystalline fluorite ceramics. *Mater Lett* 2018, **227**: 233–235.
[270] Liu ZD, Gao Q, Chang FF, *et al.* Influence of preparing conditions on the hot-pressed sintering of transparent polycrystalline fluorite ceramics. *Int J Appl Ceram Tec* 2019, **16**: 2441–2448.
[271] Yi GQ, Mei BC, Li WW, *et al.* Microstructural and optical properties of Pr^{3+}:$(Ca_{0.97}Gd_{0.03})F_{2.03}$ transparent ceramics sintered by vacuum hot-pressing method. *J Lumin* 2019, **214**: 116575.
[272] Zhi GL, Mei BC, Zhou WB, *et al.* Effects of sintering additives on preparation of CaF_2 transparent ceramics. *J Wuhan Univ Technol* 2011, **26**: 1179–1183.
[273] Chen H, Ikesue A, Noto H, *et al.* Nd^{3+}-activated CaF_2 ceramic lasers. *Opt Lett* 2019, **44**: 3378–3381.
[274] Li WW, Mei BC, Song JH. Nd^{3+},Y^{3+}-codoped SrF_2 laser ceramics. *Opt Mater* 2015, **47**: 108–111.
[275] Zhang F, Liu J, Li WW, *et al.* Dual-wavelength continuous-wave and passively Q-switched Nd,Y:SrF_2 ceramic laser. *Opt Eng* 2016, **55**: 106114.
[276] Ma FK, Su F, Zhou RF, *et al.* The defect aggregation of RE^{3+} (RE = Y, La–Lu) in MF_2 (M = Ca, Sr, Ba) fluorites. *Mater Res Bull* 2020, **125**: 110788.
[277] Siebold M, Bock S, Schramm U, *et al.* Yb: CaF_2—A new old laser crystal. *Appl Phys B-Lasers O* 2009, **97**: 327–338.
[278] Druon F, Ricaud S, Papadopoulos DN, *et al.* On Yb:CaF_2 and Yb:SrF_2: Review of spectroscopic and thermal properties and their impact on femtosecond and high power laser performance. *Opt Mater Express* 2011, **1**: 489–502.
[279] Liu XW, Mei BC, Tan GL. Transparent hexagonal Yb:$Sr_5(PO_4)_3F$ ceramics fabricated by hot pressing sintering with LiF doping. *Ceram Int* 2024, **50**: 18380–18390.
[280] Shirakawa A, Nakao H, Higashi Y, *et al.* Yb^{3+}-doped CaF_2–LaF_3 ceramic laser. In: *Advanced Solid-State Lasers Congress*. Huber G, Molton P, Eds. Paris: Optica Publishing Group, 2013: JTh5A.7.
[281] Aballea P, Suganuma A, Druon F, *et al.* Laser performance of diode-pumped Yb:CaF_2 optical ceramics synthesized using an energy-efficient process. *Optica* 2015, **2**: 288–291.
[282] Sarthou J, Duquesne JY, Becerra L, *et al.* Thermal conductivity measurements of Yb:CaF_2 transparent ceramics using the 3ω method. *J Appl Phys* 2017, **121**: 245108.
[283] Kitajima S, Higashi Y, Nakao H, *et al.* Highly efficient Yb^{3+}-doped CaF_2–LaF_3 ceramic laser. In: Proceedings of the 2016 Conference on Lasers and Electro–Optics (CLEO), 2016: 1–2.
[284] Wang C, Hao QQ, Li WW, *et al.* 575-fs passively mode-locked Yb:CaF_2 ceramic laser. *Chinese Phys B* 2020, **29**: 074205.
[285] Yang H, Qin XP, Zhang J, *et al.* The effect of MgO and SiO_2 codoping on the properties of Nd:YAG transparent ceramic. *Opt Mater* 2012, **34**: 940–943.
[286] Yi GQ, Guo XH, Wei ZS, *et al.* Concentration effect of Nd^{3+}-doped CaF_2 transparent ceramics: Structural evolution, optical transmittance and near-infrared fluorescence properties. *J Lumin* 2024, **275**: 120789.
[287] Fernández J, Oleaga A, Azkargorta J, *et al.* Nd^{3+} laser spectral dynamics in CaF_2–YF_3–NdF_3 crystals. *Opt Mater* 1999, **13**: 9–16.
[288] Zhang GR, Wu YQ. High-entropy transparent ceramics: Review of potential candidates and recently studied cases. *Int J Appl Ceram Tec* 2022, **19**: 644–672.
[289] Gludovatz B, Hohenwarter A, Catoor D, *et al.* A fracture-resistant high-entropy alloy for cryogenic applications. *Science* 2014, **345**: 1153–1158.
[290] Rost CM, Sachet E, Borman T, *et al.* Entropy-stabilized oxides. *Nat Commun* 2015, **6**: 8485.
[291] Chen XQ, Wu YQ. High-entropy transparent fluoride laser ceramics. *J Am Ceram Soc* 2020, **103**: 750–756.
[292] Samuel P, Kumar GA, Takagimi Y, *et al.* Efficient energy transfer between Ce^{3+}/Cr^{3+} and Nd^{3+} ions in transparent Nd/Ce/Cr:YAG ceramics. *Opt Mater* 2011, **34**: 303–307.
[293] Lupei V, Lupei A, Gheorghe C, *et al.* Sensitized Yb^{3+} emission in (Nd,Yb):$Y_3Al_5O_{12}$ transparent ceramics. *J Appl Phys* 2010, **108**: 123112.
[294] Saiki T, Motokoshi S, Imasaki K, *et al.* Two-pass amplification of CW laser by Nd/Cr:YAG ceramic Active mirror under lamp light pumping. *Opt Commun* 2009, **282**: 936–939.